

Nonparametric Multi-shape Modeling with Uncertainty Quantification

Hengrui Luo*

Lawrence Berkeley National Laboratory

and

Justin D. Strait†

Los Alamos National Laboratory

June 23, 2022

Abstract

The modeling and uncertainty quantification of closed curves is an important problem in the field of shape analysis, and can have significant ramifications for subsequent statistical tasks. Many of these tasks involve collections of closed curves, which often exhibit structural similarities at multiple levels. Modeling multiple closed curves in a way that efficiently incorporates such between-curve dependence remains a challenging problem. In this work, we propose and investigate a multiple-output (a.k.a. multi-output), multi-dimensional Gaussian process modeling framework. We illustrate the proposed methodological advances, and demonstrate the utility of meaningful uncertainty quantification, on several curve and shape-related tasks. This model-based approach not only addresses the problem of inference on closed curves (and their shapes) with kernel constructions, but also opens doors to nonparametric modeling of multi-level dependence for functional objects in general.

Keywords: Gaussian processes, statistical shape analysis, uncertainty quantification, functional data analysis.

*HL was supported by the Director, Office of Science, of the U.S. Department of Energy under Contract No. DE-AC02-05CH11231.

†JS was supported by the Laboratory Directed Research and Development program of Los Alamos National Laboratory under project number 20200065DR.

1 Problem Formulation

1.1 Background

A substantial number of modern data applications deal with data that possess complex structures, bringing new challenges to the use of classic statistical tools. An example of this is shape data, often extracted as boundaries of objects captured within images. Shapes have traditionally been represented either as finite point sets (Kendall, 1984; Dryden and Mardia, 2016) or planar curves (Srivastava and Klassen, 2016), with the latter dominating more modern approaches in statistics and machine learning. Geometrically, (planar) curves are either open (i.e., there are natural, unique points that can be identified as starting and ending points) or closed (i.e., any arbitrarily defined starting point on the curve is also its ending point). We focus on closed curves in this paper, which are ubiquitous in numerous applications and require additional considerations in modeling. When such data are presented as noisy realizations of some underlying curve, direct application of classical shape analysis techniques (e.g., registration) may not be suitable.

Prior to constructing statistical models for closed curves (e.g., in shape analysis), it is important to understand the uncertainty associated with estimating the underlying representative curve, given a sample of observed points. In general, uncertainty quantification is important for estimation and prediction in multiple applications. For example, in the context of experimental design, uncertainty can guide sequential sampling (Gramacy, 2020; Strait et al., 2019a; Luo et al., 2021). Unfortunately, the current literature on uncertainty quantification for these complex geometric objects focuses primarily on either open manifolds without boundaries, or univariate functional data (e.g., fMRI series (Luo et al., 2021)). Uncertainty quantification has not been studied in much detail for closed manifolds, such as \mathcal{S}^1 . One main difficulty is the proper accounting of manifold boundaries and the potential for (locally) non-trivial topological structures (Wassermann et al., 2014).

Gaussian processes (GPs) have been widely adopted as a nonparametric regression modeling tool within functional data analysis (Wang and Shi, 2014; Shi and Choi, 2011; Williams and Rasmussen, 2006), due to their flexibility in function estimation, and ability to quantify uncertainty. Closed curves can be viewed as a special, multi-dimensional form of functional data, with closed input domains (Olsen et al., 2018). Modern shape analysis methods for closed curves, such as elastic shape analysis, often consider probabilistic models which characterize variation across curves, but often ignore the uncertainty associated with fitting an individual closed curve to its observed realizations due to the assumption of *dense sampling* without consideration of noise (Kurtek et al., 2012; Huang et al., 2016). Application of these models to noisy dense samples (e.g., points extracted from image boundary methods) or sparse samples (e.g., expert landmark annotations) may not perform well without accounting for the uncertainty associated with closed curve estimation.

GP models only require a priori specification of a covariance kernel, which in essence controls the resulting smoothness of the estimated mean function and sample paths. For parameterized closed curves, a suitable covariance kernel will capture dependence between pairs of points on a single curve, where these points are simply evaluations of the curve at two different parameter values. However, models for the collection of curves typically assume independence across curves (Cheng et al., 2016; Strait et al., 2019a), which is often not an appropriate reflection of structural similarity between curves. Accounting for

between-curve dependence can help to reduce uncertainty in curve estimates, and aid in various statistical tasks such as clustering and classification. We remark further on the separate usage of the terms “curve” and “shape” in Supplementary Material A.

1.2 Challenges and Modeling Approaches

Both univariate functional data and planar curves can be viewed as parametric functions, where points in the d -dimensional Euclidean space ($d \geq 1$) are indexed by a parameter value. Parameterizations of such functions are not unique. It is standard to parameterize by arc-length, where the parameter value for a point characterizes the length of the curve traversed to that point. Unfortunately, this is not always an ideal way to parameterize closed curves for the application of functional data techniques. For example, the clustering model formulated in Zeng et al. (2019) will be overly complicated when working with curves parameterized by arc-length. Additionally, there can be a benefit in defining new parameterizations to properly associate points across curves (Zang et al., 2020; Kurtek et al., 2012).

Although there is an intrinsic relationship between closed curves (and their shapes) and univariate functional data (Olsen et al., 2018), we note that there are two major considerations in extending functional data models to closed planar curves:

- *Closedness*: The input domain for a closed curve is \mathcal{S}^1 , the unit circle, since any arbitrarily chosen starting point is also its ending point. This is different from an open curve, where the domain is \mathbb{R} . Considering parameterizations on \mathcal{S}^1 introduces challenges in modeling to ensure the resulting curve estimate is closed. This necessitates further assumptions to ensure consistency in GP modeling, since ignoring boundaries when modeling a closed manifold can introduce non-trivial consistency problems for both estimation and prediction. We solve this problem for GP models by defining a periodic covariance kernel (Duvenaud, 2014), carefully restricting the relationship between its length-scale and periodicity parameters to ensure consistency.
- *Dependence*: Closed curve data considered here have a more complex dependence structure, rendering between-curve independence assumptions inappropriate. GP models for functional data analysis (Shi and Choi, 2011; Wang et al., 2016; Greven and Scheipl, 2017; Olsen et al., 2018) usually consider univariate functions $f(x)$ with monotonic parameterizations. For closed planar curves (i.e., those with image as a subset of \mathbb{R}^2), models should be specified simultaneously on both x - and y -coordinates (two-dimensional output) as functions of one shared parameter (one-dimensional input). We solve this problem by designing a multi-level, multiple-output kernel, highlighting the sampling scheme in closed curves.

While these items are not the only methodological challenges that differentiate nonparametric models for closed planar curves (or shapes) modeling from univariate functional data, we believe these are the most pressing issues to address for proper statistical modeling.

In general, statistical approaches to modeling closed curves can be roughly classified into two groups: model-based and model-free. A *model-based approach* defines a generative, probabilistic model. For example, Stöcker and Greven (2021) generalize additive modeling

from Euclidean space to a Riemannian manifold through the local tangent bundle, allowing dependence between covariates. However, this is often at the cost of additional model parameterization and potential model misspecification. In addition, model-based approaches for closed curves and shapes typically do not consider the curve generation process (Tucker et al., 2013; Greven and Scheipl, 2017; Dareiotis and Gess, 2019). Moreover, generalization of these methods to data from different classes is challenging, with a notable exception by Kim et al. (2017). Our choice of GP modeling falls into this category.

In contrast, a *model-free approach* does not perform inference in a probabilistic sense and cannot be used to generate data. Instead, these methods focus on point estimates with no specification of a full likelihood. This includes spline models without the assumption of uncertainty or noise (Steyer et al., 2021), empirical estimation of population quantities (i.e., Karcher mean and variance), and shape registration (Kendall, 1984; Srivastava et al., 2011), all typically formulated as optimization problems without any assumption on the curve-generating process. The advantage of model-free approaches is generally efficient computation and straightforward visualization, which is advantageous for closed curve and shape analysis. However, these methods typically do not provide useful prediction nor uncertainty quantification. In addition, when no underlying model is assumed, dependence between curve locations or curves cannot be specified explicitly.

We note that there is no clear borderline between these two types of approaches. For example, the active contour model for image segmentation (Kass et al., 1988; Joshi and Srivastava, 2009; Luo and Strait, 2019) assumes an underlying distribution, but its fitting procedure mostly relates to an optimization problem. Other models have been explored to account for the dependence between closed curves. Gelfand et al. (2005) and Rodríguez et al. (2009) note that the Gaussian mixture model can characterize between-curve dependence well while still accounting for within-curve dependence with delicate hyper-parameter selection.

In this paper, we propose the use of a multiple-output GP model, with a novel multi-level covariance kernel, for estimation, prediction, and uncertainty quantification of *planar closed curves* and their corresponding *shapes*. Our approach specifies a *multi-level dependence structure*, which captures the dependence between points on closed curves (within-curve dependence) along with structural similarity across collections of closed curves (between-curve dependence). Under minimal assumptions, we obtain model-based estimates for closed curves, along with reliable *uncertainty quantification*.

Organization: First, we formally describe closed curves and their shapes, and review standard GP models, justifying their use in comparison to other approaches. Then, we describe our proposed multiple-output GP models for a single curve, followed by a collection of curves. Both of these account for structural similarity through suitable specification of a covariance kernel for closed curves, which we introduce and justify use of. Finally, we demonstrate the utility of fitting the GP model in various statistical tasks for curve and shape data. Benefits of the proposed model are illustrated throughout via numerous experiments.

2 Closed Curves, Shapes, and Parameterizations

We first introduce the types of objects being modeled in this paper, *closed curves*, and describe the notion of curve shape. A parameterized curve $\mathbf{f} : \mathcal{D} \rightarrow \mathbb{R}^d$ is a mapping from curve parameter domain \mathcal{D} into d -dimensional Euclidean space. We focus on planar curves, where $d = 2$, such that curve \mathbf{f} has coordinate functions f_1, f_2 with univariate scalar outputs. Without loss of generality, we suppose \mathbf{f} is of total length ℓ and $\mathbf{f} : [0, \ell] \rightarrow \mathbb{R}^2$ is a parameterized planar curve, indexed by parameter t . Open curves satisfy $\mathbf{f}(0) \neq \mathbf{f}(\ell)$, whereas closed curves assume $\mathbf{f}(0) = \mathbf{f}(\ell)$, for any arbitrarily defined starting point identified to $t = 0$. This consistency condition means that the domain of a closed curve should be diffeomorphic to \mathcal{S}^1 .

A natural question in modeling is how to parameterize closed curves. Typically, it is natural to restrict to parameterizations which are *monotonic*. Intuitively, monotonic parameterizations ensure that there is no stopping or reversal of motion as the curve is traversed, thus uniquely identifying each point with a time parameter value, and avoiding the situation where the same point on the curve corresponds to two different parameter values (Wang et al., 2016; Srivastava et al., 2011). Monotonicity can be introduced as a constraint when modeling curves, or as a requirement for a basis function representation. Various curve parameterizations and representations have been explored, including Gasser and Kneip (1995); Klassen et al. (2004); Srivastava and Klassen (2016). We consider two popular parameterizations for shape data, described below.

One natural choice is the *arc-length parameterization*. Given curve \mathbf{f} , its *arc-length* is the function $s(t) = \int_0^t |\mathbf{f}'(u)| du$, which evaluates the length of \mathbf{f} up to natural parameter value t . Then, the quantities $s = s(t)$ can be used as a new parameter, and $\mathbf{f}(s)$ is arc-length parameterized, with the form $s \mapsto (f_1(s), f_2(s))$, where s varies from 0 to ℓ , the total length of the curve. While closed curves do not have a natural starting or ending point, they are often provided as an ordered set of points in practice. Thus, the first point can be regarded as an arbitrarily identified starting point, and associated with both $s = 0$ and $s = \ell$, due to the closedness of the curve.

An alternative curve parameterization is the one induced by the *elastic metric*. This metric is fundamental to elastic shape analysis (Srivastava et al., 2011; Kurtek et al., 2012), where curves are flexibly re-parameterized to ensure an appropriate correspondence of features across a collection of curves. This is particularly beneficial if a parameter value does not represent a similar local feature for all curves that are modeled. Parameterizations induced by the elastic metric are found by solving the registration problem through numerical optimization, as described in Section 5.2. We present a detailed comparison of these two parameterizations in the Supplementary Materials A.

We choose to use arc-length parameterizations for fitting GPs to closed curves, in both the single curve and multiple curve settings. The justification for this is the following: prior to model fitting, we may not have dense samples from the underlying closed curve, which is assumed unknown. Even if we do have densely-sampled curve realizations, noise can severely impact elastic registration due to its reliance on derivatives. However, re-parameterization under the elastic metric is suitable once an underlying closed curve is estimated, as the proposed GP framework provides a way to bridge the gap between either sparsely sampled realizations or noisy, densely sampled realizations and smoothed, densely samples from fitted curves. Meanwhile, the parameterization induced by the elastic metric

can lead to unsatisfactory results, particularly for sparsely-sampled and/or noisy curves, as shown in Supplementary Materials J.

We note that careful algorithms for mapping between observed points and arc-length parameter values are especially critical for modeling of curves which are not densely sampled. This is important when parameterized by arc-length for GP modeling, as well as for tasks within statistical shape analysis. Curve-based methods for shape analysis (e.g., elastic shape analysis) often assume dense sampling, for which arc-length parameter values can be approximated fairly well by assigning equally-spaced parameter values on the interval $[0, \ell]$ to each point. Sparsely-sampled curves are more challenging, and we provide examples in Figure 18, along with algorithms in Supplementary Materials B, whose error bounds are provided by Theorem 3.

3 Modeling for a Single Closed Curve

Here, we further elaborate on the challenges presented in Section 1, with a focus on GP modeling of a single closed curve and its shape (class). A basic discussion of GPs can be found in the Supplementary Materials C and Williams and Rasmussen (2006).

Suppose that we observe sample points from a single closed curve, which we assume to be parameterized by the arc-length parameter s . In other words, we observe n input-output combinations (s_i, \mathbf{y}_i) , where $s_i \in \mathbb{R}$ is the one-dimensional parameter value associated with point $\mathbf{y}_i = (y_{i1}, y_{i2})^T \in \mathbb{R}^2$. The points are assumed to have been generated from the (unknown) underlying curve \mathbf{f} with coordinate functions f_1, f_2 . Let $\mathbf{s} = (s_1, \dots, s_n)^T$ be the vector of input arc-length parameter values, and \mathbf{Y} contain the full two-dimensional output values:

$$\mathbf{Y} = \begin{pmatrix} y_{11} & y_{12} \\ \vdots & \vdots \\ y_{n1} & y_{n2} \end{pmatrix} = \begin{pmatrix} \mathbf{y}_1^T \\ \vdots \\ \mathbf{y}_n^T \end{pmatrix} = (\mathbf{y}_{\cdot 1} \quad \mathbf{y}_{\cdot 2}) \in \mathbb{R}^{n \times 2}. \quad (1)$$

To clarify the notation, $\mathbf{y}_i \in \mathbb{R}^2$ represents the Euclidean coordinates of the output for input s_i , whereas $\mathbf{y}_{\cdot d} \in \mathbb{R}^n$ represents all n output values across dimensions $d \in \{1, 2\}$. We consider the following general model with additive noise:

$$\begin{pmatrix} y_{i1} \\ y_{i2} \end{pmatrix} = \begin{pmatrix} f_1(s_i) \\ f_2(s_i) \end{pmatrix} + \begin{pmatrix} \epsilon_{i1} \\ \epsilon_{i2} \end{pmatrix} \iff \mathbf{y}_i = \mathbf{f}(s_i) + \boldsymbol{\epsilon}_i, \quad (2)$$

where $\boldsymbol{\epsilon}_i = (\epsilon_{i1}, \epsilon_{i2})^T$ is the error vector and $\mathbf{f} = (f_1, f_2)$ is unknown. Note that \mathbf{f} maps one-dimensional input (i.e., arc-length) to a two-dimensional output (i.e., x - and y -coordinates). We use the Python module `GPFlow2` (Matthews et al., 2017; van der Wilk et al., 2020) for implementations of the GP model.

In this paper, we view the coordinates $(f_1(s), f_2(s))$ directly as the (x, y) coordinates in \mathbb{R}^2 . This allows uncertainty estimates to be most natural and directly interpretable as a function of location in Euclidean space. A drawback of this is that uncertainty quantification is only performed with respect to the coordinate system along the x - and y -axes, rather than intrinsically with respect to the underlying curve.

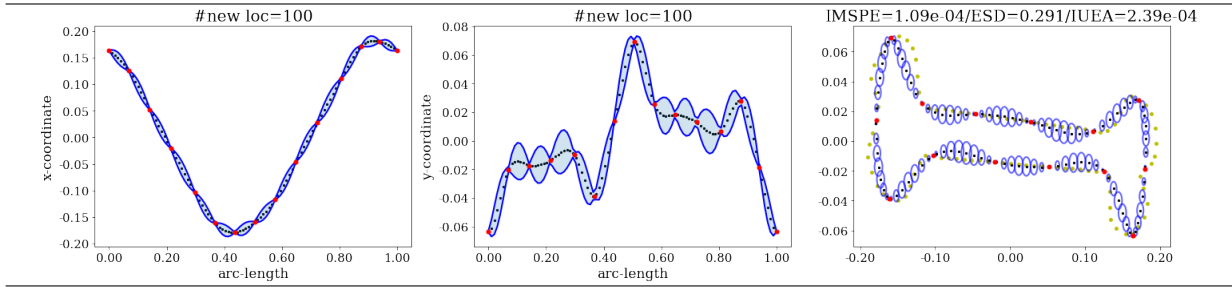


Figure 1: **Single-output GP model.** Bone curve from MPEG-7 (Bai et al., 2009), observed at 15 "equally-spaced" sample points, and modeled using separate single-output GPs. The first two columns represent coordinate function fits, with prediction in black and 95% pointwise prediction intervals represented as blue bands. The final column shows the overall curve fit with uncertainty ellipsoids, with details described below.

Figure conventions. Ellipsoid plots in the rest of the paper follow the same convention, with sample points in red, predicted mean in black, and the true curve in yellow. Uncertainty is depicted by blue ellipsoids at each prediction point, with principal axes driven by pointwise standard deviations for each coordinate. Integrated mean squared prediction error (IMSPE) and elastic shape distance (ESD) between predicted mean and true curves, and integrated uncertainty ellipsoid area (IUEA), is reported at the top (see Supplementary Materials I for detailed definitions). Unless otherwise specified, all models are fit using periodic Matern 3/2 kernel with an additional constant kernel (for numerical purposes), and ellipses span 1 standard deviation.

3.1 Single-output Gaussian Processes for a Single Curve

A simple way to extend the single-output GPs to multiple dimensions is to fit separate, independent GPs to each output dimension (i.e., separate coordinate functions), so that we obtain the finite-dimensional model in (2).

In particular, f_1, f_2 are assumed to be Gaussian processes with kernel functions k_1, k_2 and ϵ_1, ϵ_2 are independent Gaussian noise terms. The dependence within the d -th coordinate function, for $d = 1, 2$, is $\text{Cov}(f_d(s_i), f_d(s_j)) = k_d(s_i, s_j)$ for n different sample points from the curve indexed by $i, j = 1, \dots, n$. This formulation allows k_1 and k_2 to be independently specified, with possibly different covariance kernels or parameters for each dimension (e.g., ARD, Chapelle et al. (2002)). For the vector $\mathbf{f}(s_i)$, the joint kernel $K = k_1 \otimes k_2$ produces a 2×2 covariance matrix, $K_{\mathbf{f}}(s_i, s_j) = \text{diag}(k_1(s_i, s_j), k_2(s_i, s_j))$, and the covariance matrix for ϵ_i can be written as $\Sigma = \text{diag}(\sigma_{\epsilon_1}^2, \sigma_{\epsilon_2}^2)$. Zeros on the off-diagonals of these covariance matrices imply that there is no dependence between coordinate functions.

Figure 1 shows the results of fitting separate single-output GP models for each dimension for a bone from the MPEG-7 dataset (Bai et al., 2009). The left and middle panels show the predictive mean and 95% confidence intervals illustrated by the pointwise upper and lower confidence bands for the estimated x - and y -coordinate functions. The predictive mean and variances can be combined to show the GP model estimates for a closed curve, as shown in the right panel, with uncertainty represented by (the volumes of) ellipsoids (described in the caption of Figure 1). This plot shows a pattern similar to traditional GP regressions in one dimension, where uncertainty shrinks near the observed point.

3.2 Closedness and Periodic Kernels

As above, our data are sampled from an underlying, unknown closed curve \mathbf{f} which is parameterized by arc-length s . The challenge of using this parameterization for closed curves is the following: if ℓ is the total length of curve \mathbf{f} , then under an arc-length parameterization, parameter value $s = 0$ should also be mapped to the same point on the curve as the parameter value $s = \ell$. In practice, the first observed point sampled from the underlying curve can naturally be associated with $s = 0$, but as discussed earlier, we must keep in mind that the domain of a closed curve is actually \mathcal{S}^1 and this starting point is arbitrarily chosen. Thus, we must take care to recognize that the model fitting should be invariant to cyclic permutations of the rows of \mathbf{Y} , i.e., the ordering of the observed points.

There are two major approaches to handling the additional assumption of periodicity. First, the model can be restricted to a single period by specifying a parametric periodic model, with coinciding starting and ending points. An example of this is trigonometric regression (Eubank and Speckman, 1990), where trigonometric functions are used as basis functions to account for periodicity (Fisher et al., 1993; Fisher, 1995). However, estimating regression parameters associated with periodic basis functions can be difficult, and the accompanying Gibbs phenomena introduces an identifiability problem (Quinn, 1989; Eubank and Speckman, 1990). Alternatively, one can fit a fully nonparametric model for the full closed manifold, adding periodic constraints. We take the latter approach for the following reason.

For (univariate) functional data, typically the monotonic parameter values are known (e.g., time points). Thus, its range of parameter values can be bounded based on those corresponding to the starting and ending points, and we can add more refined sample points in the domain without changing this range. However, for a closed curve, parameter values are generally not known or provided; as mentioned earlier, it is most natural to parameterize such curves by arc-length. Since estimating a curve’s total length depends on discretization, the range of the natural arc-length parameter will not be fixed; thus, standardization is needed after every refinement. This means that restricting estimation to within one period is impractical. Therefore, a closed curve parameterization should not only be monotonic, as we have assumed for open curves, but also *periodic*.

We incorporate periodic constraints by specifying a periodic covariance kernel (Duvenaud, 2014) with appropriate constraints on hyperparameters, for the following reason. Suppose a closed curve $\mathbf{f}(s) = (f_1(s), f_2(s))$ is assumed to have an extended domain $[0, \infty)$, such that the curve is re-traced after every interval of length ℓ . Simply coinciding starting and ending points and restricting the model forces $\mathbf{f}(0) = \mathbf{f}(\ell)$, but there is no guarantee that the two identical pairs of points $\mathbf{f}(0), \mathbf{f}(\delta)$ and $\mathbf{f}(\ell), \mathbf{f}(\ell + \delta)$ are perfectly correlated. Ensuring this consistency in the dependence structure is important because the underlying curve \mathbf{f} is unknown, meaning that its total length ℓ must be estimated. Based on this observation, \mathcal{S}^1 is observed to be a more appropriate modeling domain (Srivastava et al., 2011; Olsen et al., 2018).

Definition 1. (*Periodic covariance kernels, MacKay et al. (1998), Williams and Rasmussen (2006), Sections 4.2 and B.1*) The canonical periodic covariance kernel (with period

τ) is defined as:

$$k_{(\sigma^2, \rho, \tau)}(s_i, s_j) = \sigma^2 \exp \left(-\frac{1}{\rho} \sin^2 \left(\frac{\|s_i - s_j\|}{\tau/\pi} \right) \right), \quad (3)$$

for hyperparameters $\sigma^2 \in (0, \infty), \rho \in (0, \infty), \tau \in (0, \infty)$. We require that there is an isometry between $\|\cdot\|$ and arc-length metric on \mathcal{S}^1 .

Note that the canonical periodic covariance kernel is a mapping of the radial basis function kernel, obtained by mapping inputs onto \mathcal{S}^1 (MacKay et al., 1998). Periodic covariance kernels based on other base kernels (e.g., the Matern family) can be derived in a similar fashion. As shown in Minh et al. (2006), the canonical periodic kernel defined in $\mathcal{D} = \mathbb{S}^1$ is a Mercer kernel with respect to the spherical harmonics, whose eigenvalues can be computed, and its spectrum comes with perturbation bounds (Braun, 2006).

Classically, this construction of warping by the sine function is found in circular statistics (Fisher, 1995). The use of this kernel requires the selection of the period τ , which is difficult in practice. One could treat τ as a hyperparameter to be estimated in a parametric model, but this is problematic because of the presence of many local optima, due to identifiability issues introduced by the sine function: any estimate of the period with the form $\hat{\tau} + 2\pi \cdot \mathbb{N}$ is valid. This problem can be traced back to Fisher (1929), and also appears in periodicity estimation for time series (Siegel, 1980; Ahdesmäki et al., 2005) and topological data analysis (Luo et al., 2021). We do not attempt to address this rather complicated problem here, yet point out that discussions in Sections 6.2 and 6.3 of Fisher (1995) indicate that it may affect the statistical power of certain tests. Instead of optimizing over τ , we choose to set τ close to the total length of the curve \mathbf{f} by an estimate based on the length of a piecewise-linear curve connecting the observed sample points. As shown in Figure 3, model fits are generally robust under this heuristic.

Note that the length scale in a stationary kernel (e.g., the hyperparameter ρ in an RBF kernel) does not have the same interpretation as the period in its corresponding periodic kernel (e.g., the hyperparameter τ in (3)). The length scale drives the strength of correlation between s_i, s_j , while the period model recurrence of a certain pattern. For a periodic kernel, the magnitude of correlation between two points depends on both the length scale and period. The following result allows us to compare the behavior of a periodic kernel with its non-periodic counterpart.

Theorem 1. *Given true curve length ℓ , suppose inputs $s_i, s_j \in \mathcal{D}$ are within a period, i.e., $0 \leq r \leq \tau$ for $r = \|s_i - s_j\|$. Then,*

$$\sigma^2 \left(1 - \frac{\pi^2 \ell^2}{4\rho\tau^2} \right) \leq k_{(\sigma^2, \rho, \tau)}(s_i, s_j) \leq \sigma^2 \left(1 + \frac{1}{64} \left(\frac{2\pi^4}{\rho^2\tau^4} + \frac{4\pi^4}{3\rho\tau^4} \right) \ell^4 \right).$$

Proof. See Supplementary Materials D. □

Using this theorem, we can deduce some required and practical bounds between kernel hyperparameters. First, the consideration of consistency requires $\tau \leq \ell$, since we want the dependence to be identical after fully tracing the closed curve. This ensures identifiability of length scale and period hyperparameters. Furthermore, no two points on the curve can be more than arc-length distance $\ell/2$ apart along the closed curve. Thus, heuristically, the

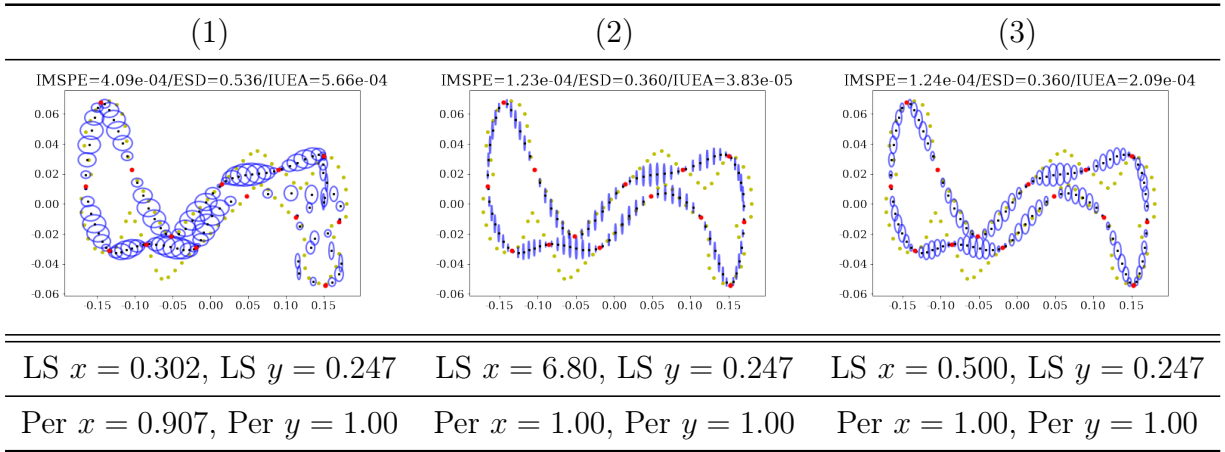


Figure 2: Effect of length scale constraints with periodicity estimates on GP model fits. Bone curve from MPEG-7 observed at 15 points. Panel (1) shows the identifiability issue when neither the length scale nor period is constrained. Panel (2) fixes the period to the estimated arc-length, with length scale still unconstrained. Panel (3) fixes the period and constrains the length scale by $\rho \leq \tau/2$. Estimated length scale (LS) and period (Per) hyperparameters are reported for the separate single-output GP fits for the coordinates x, y .

correlation should decay to nearly zero before the distance $\ell/2$, to allow two points to be uncorrelated. Finally, from empirical studies, we strongly suggest $\rho \lesssim \frac{\tau}{2}$ to ensure identifiability between these two parameter estimates. For most kernels, we find this constraint to be suitable in practice, as shown by the trade-off between length scale and period in the Supplementary Materials, Figure 16.

Figure 2 shows separate single-output GPs model fits (i.e., Section 3.1) with a stationary periodic kernel to a different bone shape. The fit is rather poor when there is no constraint on length scale and the period is estimated: while the predictive mean exhibits interpolation behavior with the expected decreased uncertainty near observed points, the period in the x -coordinate does not match that of the y -coordinate, resulting in an unusual fit on the bone’s right side. Fixing the period (without length scale constraints) improves the overall fit. However, the length scale hyperparameter increases significantly in the x -coordinate, resulting in its uncertainty estimates being much smaller than those in the y -coordinate. If the length scale hyperparameter is constrained to half of the estimated arc-length (i.e., the fixed period) as in panel (3), we obtain an improved fit in which uncertainty is properly reflected in both the x - and y -coordinates of the curve. This echoes the observation in Figure 3 that the period τ should be reasonably close to the total curve length ℓ . Choosing $\tau \ll \ell$ results in poor fits, and choosing $\tau \gg \ell$ typically yields over-smoothed predictions.

In general, when defining kernels on arbitrary manifolds, the often-convenient Bochner theorem may not be suitably applied to ensure kernels are positive semi-definite. As pointed out by Borovitskiy et al. (2020), kernel methods including GP models cannot be applied directly to closed manifolds. However, with careful constraints, the periodic kernel can be used for closed planar curves with no issue.

Theorem 2, based on Koepernik and Pfaff (2021), ensures model consistency when coordinate functions of the underlying closed curve lie in a space induced by the periodic

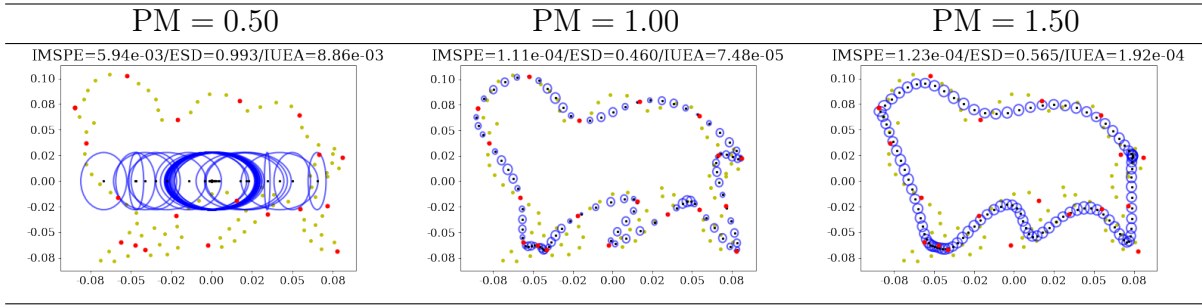


Figure 3: **Effect of periodicity specification on GP model fits.** Camel curve from MPEG-7, observed at 20 points. Here, the period hyperparameter is fixed to be the arc-length (estimated from the true curve) multiplied by a scalar denoted PM, and length scale is constrained accordingly.

kernel. We prove the theorem for a single curve, but expect the argument to hold for multiple curves.

Theorem 2. Let $f_1, f_2 : \mathcal{D} \rightarrow \mathbb{R}$ be the true coordinate functions for a closed curve. Also, let $\hat{f}_{1,n}, \hat{f}_{2,n} : \mathcal{D} \rightarrow \mathbb{R}$ be the mean coordinate functions based on a sample of size n on \mathcal{D} , as in (10), with additive Gaussian noise (i.e., (4) in Koepernik and Pfaff (2021)) parameterized by variance σ_ϵ^2 . Assume that the following assumption holds:

- (1) \mathcal{D} is homeomorphic to \mathcal{S}^1 , with a metric isometric to the arc-length metric on \mathcal{S}^1 .
- (2) Stationary periodic kernel $k_{(\sigma^2, \rho, \tau)}$ defined in (3) has finite, nonzero hyperparameter values (σ^2, ρ, τ) .
- (3) The sequence of sample points indexed by sample size n is a dense sequence in \mathcal{D} .

Then, the following statements hold:

(A) If f_1, f_2 belong to a reproducing kernel Hilbert space (Aronszajn, 1950) defined by $k_{(\sigma^2, \rho, \tau)}$, then $\hat{f}_{1,n} \xrightarrow{L_2} f_1$ and $\hat{f}_{2,n} \xrightarrow{L_2} f_2$.

(B) If f_1, f_2 are continuous with respect to the topology induced by $\|\cdot\|$ in Equation (3) for $k_{(\sigma^2, \rho, \tau)}$, then $\sup_{s \in \mathcal{D}} |\hat{f}_{1,n}(s) - f_1(s)| \xrightarrow{L_1} 0$ and $\sup_{s \in \mathcal{D}} |\hat{f}_{2,n}(s) - f_2(s)| \xrightarrow{L_1} 0$.

Proof. See Supplementary Materials E. □

In Theorem 2, the first assumption requires a closed domain, and the second assumption allows use of Theorem 1 under appropriate period constraints. The third assumption requires dense sample points on the closed curve, and is crucial to the theorem holding true. Increasing the number of sample points in a curve leads to improved GP modeling, as shown in the top row of Figure 4. A slightly weaker assumption on the sampling scheme, where the distance between consecutive points converges to zero, is also important in algorithmic consistency, as shown in Theorem 3 (in Supplementary Materials B).

However, for a finite number of sample points, the curve sampling scheme is still important to minimize the model prediction variance. Pointwise uncertainty estimates (depicted by ellipses at prediction points) will decrease as the arc-length distance between observed sample points decreases (which occurs when the number of sampling points increases). The top panel of Figure 4 assumes an equally-spaced sampling scheme, which is most intuitive. We define equally-spaced to be with respect to the arc-length metric along the underlying curve. The bottom panel of Figure 4 shows clustered sampling, which results in unusual GP

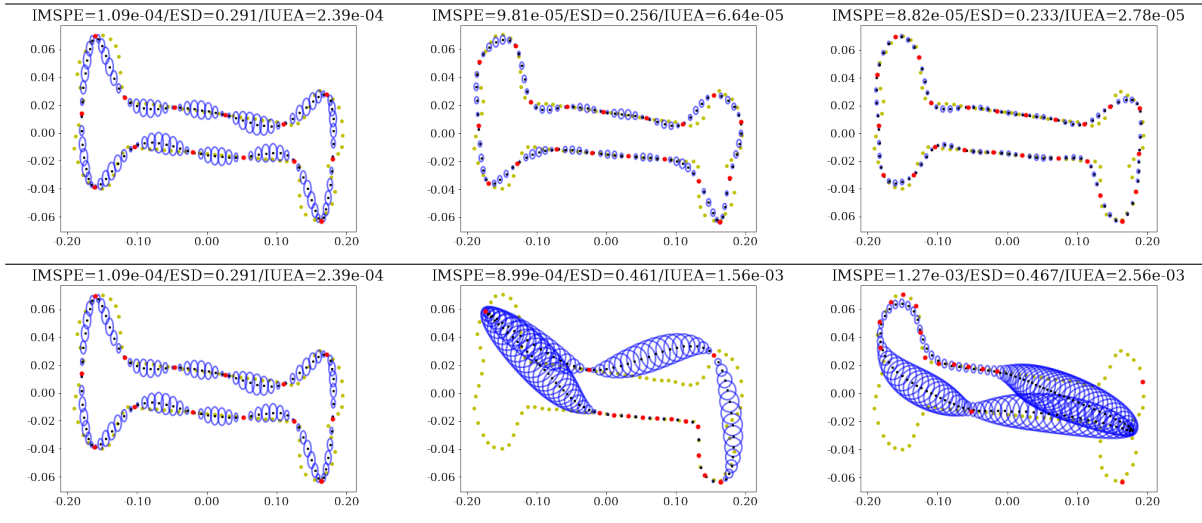


Figure 4: **Effect of sampling scheme on GP model fits.** Bone curve from MPEG-7, modeled using separate single-output GPs. (Top row) From left to right, the same model is fit based on an equally-spaced sampling scheme with 15, 20, and 25 observed sample points. (Bottom row) The same model is fit on 15 sampling points, with an equally-spaced sampling scheme on the left, and two different cluster sampling schemes in the right two panels.

fits with substantial uncertainty in regions of the underlying curve which are not adequately sampled.

Finally, we remark on separate single-output GP model fits under various periodic stationary covariance kernels. GPs have the advantage of explicitly controlling the smoothness of the mean function explicitly through the choice of covariance kernels (Cramér and Leadbetter, 2013), which is crucial for subsequent analyses, e.g., in elastic shape analysis (Kurtek et al., 2012). Figure 5 shows the fits of a butterfly curve under three different periodic stationary kernels: RBF, Matern 3/2, and Matern 1/2, which assume high to low smoothness, respectively, in the underlying curve fit. This butterfly has been perturbed pointwise by uncorrelated bivariate Gaussian noise. Note that the RBF kernel fit does not appear to be suitable for modeling this butterfly due to its overly smooth behavior, which results in two self-intersections in the predicted mean curve. The Matern 3/2 kernel yields a fit with the rightmost self-intersection resolved, and increased uncertainty. The Matern 1/2 kernel results in the last smooth predicted mean curve, at the cost of increased uncertainty (as represented by ellipsoids). However, this sacrifice may be worthwhile given the limited number of observed sample points here, as both self-intersections disappear.

In general, the choice of kernel should consider both the sampling scheme of points from the underlying curve, as well as the general smoothing requirements. When there are sparse sample points and a smooth fit is desirable, we suggest using smooth, periodic stationary kernels. When there are dense sample points and a detailed closed curve fit is needed, we suggest less smooth, periodic stationary, or even nonstationary kernels (see Supplementary Materials F).

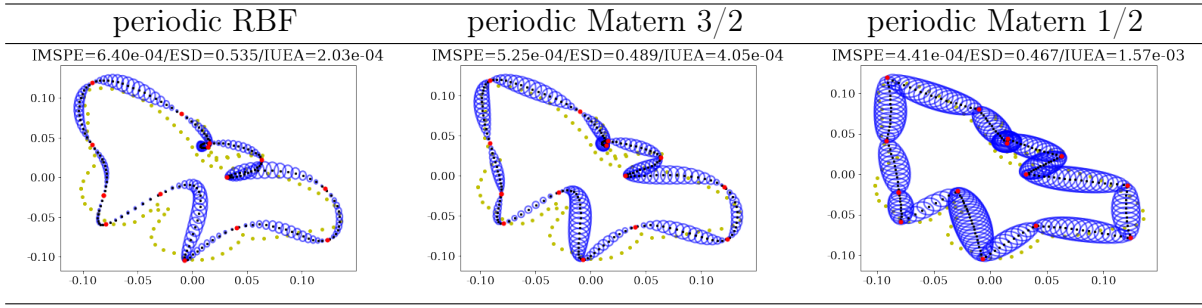


Figure 5: **Effect of kernel choices on GP model fits.** Butterfly curve from MPEG-7 sampled at 20 points, perturbed pointwise by uncorrelated bivariate normal noise with standard deviation 0.008, and modeled using separate single-output GPs under various periodic stationary kernels.

3.3 Multiple-output Gaussian Processes for a Single Curve

A significant drawback to the separate single-output GP model is its lack of ability to capture correlation between a curve’s two coordinate functions. It is natural to assume model outputs are correlated, since knowledge of the x -coordinate at parameter value s can help in inferring the corresponding y -coordinate, particularly after accounting for dependence between different input parameter values. We deem this consideration *within-curve coordinate dependence*, as dependence between coordinate functions models the concurrent changes of the two coordinates of a point on a fixed curve.

To incorporate within-curve coordinate dependence, let $K_{\mathbf{f}}$ be a kernel such that for $s_i, s_j \in \mathcal{D}$, we can express the covariance matrix between coordinate function outputs in general as:

$$K_{\mathbf{f}}(s_i, s_j) = \begin{pmatrix} \text{Cov}(f_1(s_i), f_1(s_j)) & \text{Cov}(f_1(s_i), f_2(s_j)) \\ \text{Cov}(f_2(s_i), f_1(s_j)) & \text{Cov}(f_2(s_i), f_2(s_j)) \end{pmatrix}. \quad (4)$$

Thus, one can identify $K_{\mathbf{f}}$ by specifying a general expression for $\text{Cov}(f_d(s_i), f_{d'}(s_j))$, with $d, d' \in \{1, 2\}$. A common approach is to specify a *separable kernel*: define $K_{\mathbf{f}} = k \otimes k_D$ as the Kronecker product of the scalar kernels k and k_D , where k is the input kernel (i.e., chosen to be a periodic stationary kernel in light of Section 3.2) and k_D is the within-curve coordinate kernel. This means that $\text{Cov}(f_d(s_i), f_{d'}(s_j)) = k(s_i, s_j)k_D(d, d')$. If both k and k_D are valid kernels (i.e., symmetric and positive semi-definite), then their product also satisfies the required properties of kernels.

In the separate single-output GP model of Section 3.1 (where the coordinate functions are uncorrelated), (4) is assumed to have off-diagonal entries equal to zero, meaning that $k_D(d, d') = \delta(d, d')$ for Kronecker delta δ . However, suitable modifications of the within-curve coordinate kernel k_D can flexibly allow correlation between coordinates. We note that a separable kernel assumes that similarity for multiple outputs can be characterized independently across every dimension. In the setting of closed curves, this means that we are implicitly assuming that k_D remains the same across all possible pairs of inputs $s_i, s_j \in \mathcal{D}$. This assumption nicely decomposes correlation into separate components attributed between inputs and between coordinate functions. Unlike the periodic requirement for within-coordinate dependence, this hierarchy can be extended to higher dimensions. Alternatively, one could construct more complex interactions between kernels k and k_D .

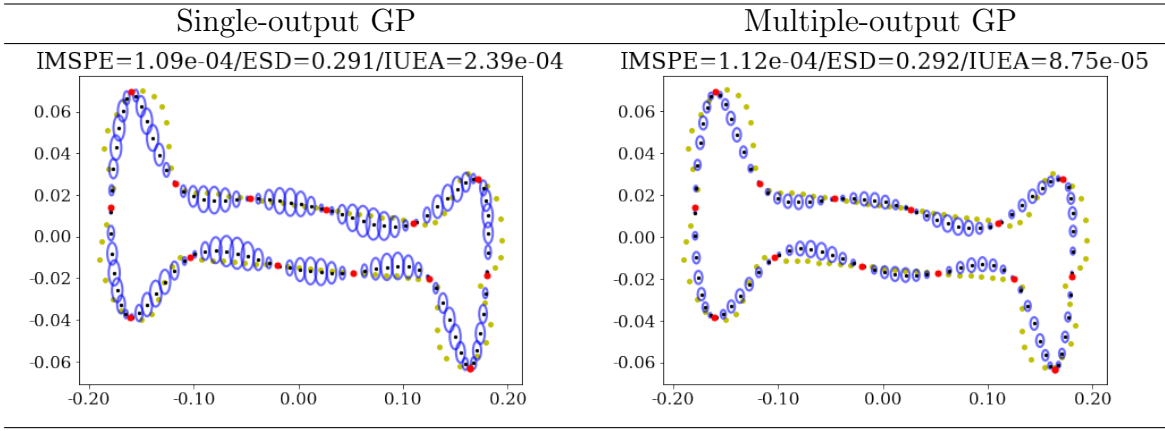


Figure 6: **Comparisons between single-output and multiple-output GP models.** Bone curve from MPEG-7, modeled using separate single-output GPs (left) and a multiple-output GP (right).

Note that the matrix in (4) can be written as $k(s_i, s_j) \cdot D$ where D is a 2×2 symmetric and positive semi-definite matrix such that $D_{d,d'} = k_D(d, d')$. The matrix D is often referred to as *coregionalization matrix*. Estimation of D means estimating its entries subject to the constraint of symmetry and positive semi-definiteness, and quantifies the dependence accounted for between a single curve’s coordinate functions. The above construction of product kernel follows from Bonilla et al. (2007); however, more flexible coregionalizations, such as additive kernels $k + k_D$ or convolution kernels $k \star k_D$ present other possible dependence across different outputs. In what follows, we focus on the product kernel in the current paper. To ensure positive semidefiniteness, note that the Python module `GPFlow2` (Matthews et al., 2017; van der Wilk et al., 2020) parameterizes the coregionalization matrix as $D = WW^T + \text{diag}(\kappa)$, where W is a $2 \times r$ matrix with $\text{rank}(W) = r \leq 2$ and κ is a 2-dimensional vector. In general, increasing the rank yields more flexible matrices D .

Figure 6 compares separate single-output GP fits to a multiple-output GP fit for the same bone from Figure 1. This fit use a periodic kernel k , with the multiple-output fit using the specification above (i.e., estimates coregionalization matrix D). Note that both models yield similar predicted mean curves: the coregionalization model borrows information between coordinates to generally reduce predictive uncertainty, while the input kernel controls the overall smoothness.

4 Modeling for Multiple Closed Curves

In this section, we extend the multiple-output Gaussian process model from Section 3 to the multiple-curve setting. An important contribution of this section is the specification of a covariance kernel which is not only separable across input parameter values and curve dimension (as in the single curve setting), but also across curves themselves. Before proceeding to discussion of the multi-level kernel specification, we note that when specifying a joint model for multiple curves, the sample points from these curves should be pre-processed (See Supplementary Materials H).

Suppose that we observe sample points from J closed curves, all of which are assumed to be arc-length parameterized. In other words, for curve j , we observe n_j input-output

combinations $(s_i^{(j)}, \mathbf{y}_i^{(j)})$, where $s_i^{(j)} \in \mathbb{R}$ is the arc-length parameter value for point $\mathbf{y}_i^{(j)} = (y_{i1}^{(j)}, y_{i2}^{(j)})^T \in \mathbb{R}^2$, which is assumed to have been sampled from the (unknown) underlying curve $\mathbf{f}^{(j)} = (f_1^{(j)}, f_2^{(j)})$. The number of observed sample points n_j can vary by curve j , such that the vector of arc-length parameters $\mathbf{s}^{(j)} = (s_1^{(j)}, \dots, s_{n_j}^{(j)})^T$ is computed with respect to curve j , thus allowing them to be curve-specific, i.e.:

$$\mathbf{Y}^{(j)} = \begin{pmatrix} \mathbf{y}_{1\cdot}^{(j)} \\ \vdots \\ \mathbf{y}_{n_j\cdot}^{(j)} \end{pmatrix} = \begin{pmatrix} y_{11}^{(j)} \\ y_{12}^{(j)} \\ \vdots \\ y_{n_j1}^{(j)} \\ y_{n_j2}^{(j)} \end{pmatrix} = \begin{pmatrix} f_1^{(j)}(s_1) \\ f_2^{(j)}(s_1) \\ \vdots \\ f_1^{(j)}(s_{n_j}) \\ f_2^{(j)}(s_{n_j}) \end{pmatrix} + \begin{pmatrix} \epsilon_{11}^{(j)} \\ \epsilon_{12}^{(j)} \\ \vdots \\ \epsilon_{n_j1}^{(j)} \\ \epsilon_{n_j2}^{(j)} \end{pmatrix} \in \mathbb{R}^{2n_j}, \mathbf{Y}^{(j)} = \mathbf{f}^{(j)}(\mathbf{s}^{(j)}) + \boldsymbol{\epsilon}^{(j)}. \quad (5)$$

For curve j , $\mathbf{y}_i^{(j)} \in \mathbb{R}^2$ is the observed sample point at the input parameter $s_i^{(j)}$, whereas $\mathbf{y}_d^{(j)} \in \mathbb{R}^{n_j}$ is the vector of all n_j output values in dimension $d \in \{1, 2\}$.

In the multiple curve setting, separate multiple-output GP models can be specified for each curve using Section 3. For curve j , we can construct different covariance structures $K_{\mathbf{f}}^{(j)}$: either diagonal (to reflect independent outputs) with periodic kernels on its arc-length parameter inputs (to address closedness), or separable as in (4) to incorporate within-curve coordinate dependence through coregionalization. In either case, let $\Sigma^{(j)} = \text{diag}(\sigma_{\epsilon 1}^{2(j)}, \sigma_{\epsilon 2}^{2(j)})$ be the accompanying noise covariance matrix, and accounting for within-curve coordinate dependence through coregionalization can result in tighter prediction bands when fitting GPs. However, separate specification of $K_{\mathbf{f}}^{(j)}$ across curves $j = 1, \dots, J$ results in an added assumption of between-curve independence.

In order to incorporate between-curve dependence, we can borrow the coregionalization specification used in Section 3.3 to further exploit structural similarities across curves. This between-curve dependence is conditional on existing dependence structures between inputs (parameter values) and curve-specific outputs (dimensions). More specifically, we specify the following multi-level dependence structure:

1. *Within-coordinate dependence for a fixed curve:* This reflects the dependence between points $s, s' \in \mathcal{D}$ for a single fixed coordinate function $f_d^{(j)}$ of curve j , denoted by $\text{Cov}(f_d^{(j)}(s), f_d^{(j)}(s'))$ for $d = 1, 2$. For a closed curve, this means use of the periodic kernel $k_{(\sigma^2, \rho, \tau)}(s, s')$.
2. *Within-curve coordinate dependence for a fixed curve:* This reflects the dependence between the coordinate functions of the curve j . When both coordinate functions $f_d^{(j)}, f_{d'}^{(j)}$ are evaluated at a parameter value s , we denote this dependence by $\text{Cov}(f_d^{(j)}(s), f_{d'}^{(j)}(s))$, for $d, d' \in \{1, 2\}$ with $d \neq d'$.
3. *Between-curve dependence:* This reflects the dependence between curves $j, j' \in \{1, \dots, J\}$ with $j \neq j'$, evaluated at a vector of parameter values $\mathbf{s}^{(j)}, \mathbf{s}^{(j')}$. We denote this dependence by $\text{Cov}(\mathbf{f}^{(j)}(\mathbf{s}^{(j)}), \mathbf{f}^{(j')}(\mathbf{s}^{(j')}))$.

The first two sources of dependence are identical to the dependence structure for a single curve, while the third source is added for joint modeling of multiple curves.

To specify the full Gaussian process model which incorporates this multi-level dependence structure across all J curves, we can vectorize as follows:

$$\begin{pmatrix} \mathbf{Y}^{(1)} \\ \vdots \\ \mathbf{Y}^{(J)} \end{pmatrix} = \begin{pmatrix} \mathbf{f}^{(1)}(\mathbf{s}^{(1)}) \\ \vdots \\ \mathbf{f}^{(J)}(\mathbf{s}^{(J)}) \end{pmatrix} + \begin{pmatrix} \boldsymbol{\epsilon}^{(1)} \\ \vdots \\ \boldsymbol{\epsilon}^{(J)} \end{pmatrix} \in \mathbb{R}^{2n_j}. \quad (6)$$

We choose to specify a separable kernel: for scalar kernels k , k_D , and k_C , let $K = k \otimes k_D \otimes k_C$ have elements $\text{Cov}\left(f_d^{(j)}(s), f_{d'}^{(j')}(s')\right) = k(s, s')k_D(d, d')k_C(j, j')$. The within-curve coordinate dependence kernel k_D is specified in the same way as Section 3.3, such that coregionalization matrix D has entries $D_{d,d'} = k_D(d, d')$, constrained to yield a symmetric and positive semi-definite matrix. Due to the assumption of separability, note that k_D is independent of the curve index j , which fixes the between-dimension dependence across all curves. However, this can be replaced with more general kernels. To incorporate between-curve dependence, we specify a between-curve scalar kernel k_C such that its evaluation $k_C(j, j')$ for $j, j' \in \{1, \dots, J\}$ measures the similarity between curves $\mathbf{f}^{(j)}$ and $\mathbf{f}^{(j')}$. Similar to k_D , a simple choice is to use the intrinsic coregionalization model, defining a $J \times J$ -dimensional coregionalization matrix C such that $C_{j,j'} = k_C(j, j')$, constrained to be symmetric and positive semi-definite.

Fitting the joint multiple-output GP model with the above separable kernel amounts to estimating kernel hyperparameters of k, k_D, k_C ; for coregionalization matrices C and D , this means estimating their entries subject to required constraints. Based on the three-dimensional kernel K , one can compute the corresponding covariance matrix of all observed sample points across all J curves, which has dimension $2N$ for $N = \sum_{j=1}^J n_j$.

Figure 7 shows a comparison of separate and joint multiple-output GP fits, where each of the three camels is cluster sampled in a different region: the first around the humps, the second around the front legs, and the third around the rear legs and tail. In all cases, curves are re-scaled to unit length and zero-centered; the right panel also rotates the last two camels to match the first camel prior to model fitting, whereas the middle panel does not perform this step. (see Supplementary Materials Section H.)

From this figure, we note the further reduction in predictive uncertainty and improved mean curve prediction under joint modeling of the three curves, as each curve has detailed information in different regions of the camel. In addition, note that rotation pre-processing actually impacts fits quite differently; for instance, the first and second camels have more distinct rear legs, and apparent self-intersections in the predicted mean for the second camel disappear when properly rotationally aligned.

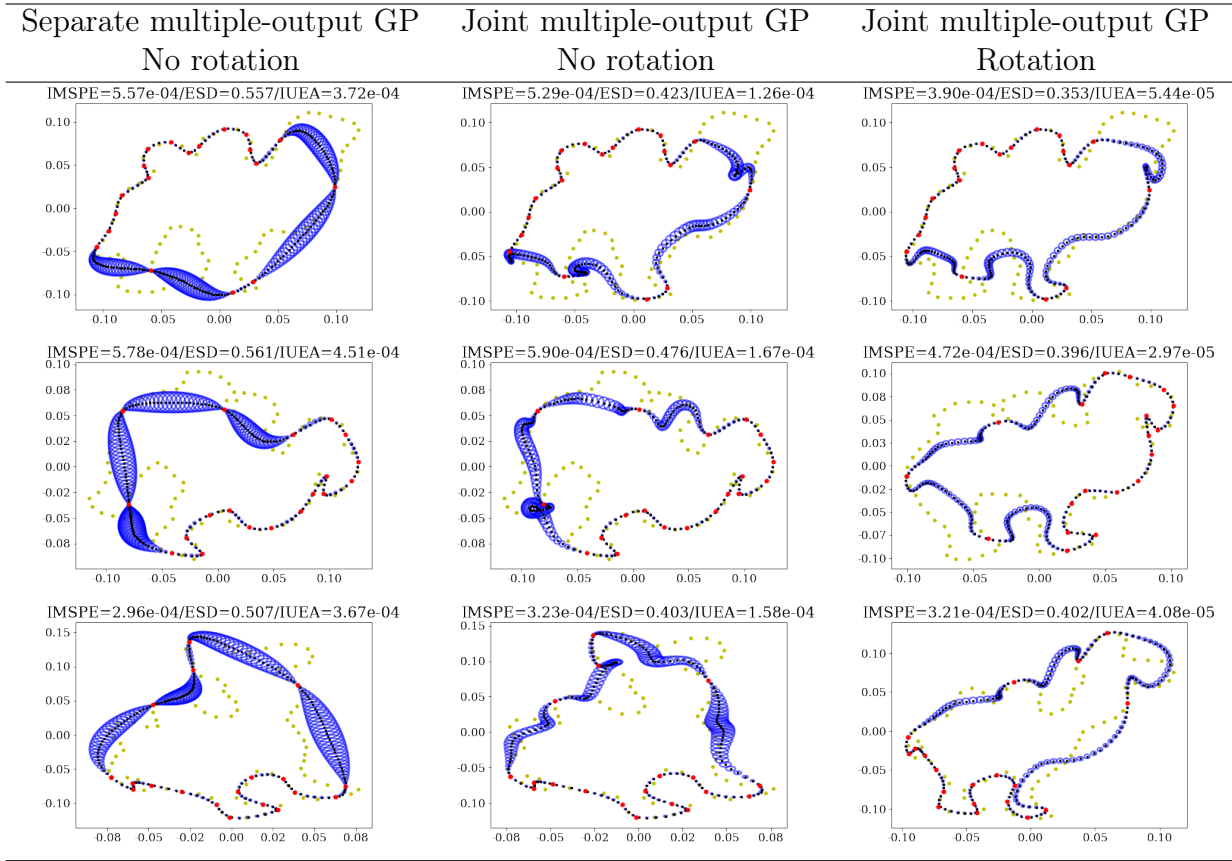


Figure 7: **Comparisons between separate multiple-output and joint multiple-output GP models for multiple curves.** Three camel curves from MPEG-7, modeled using 20 sample points fitted by separate multiple-output GPs for each curve (left) and a jointly fit multiple-output GP without (middle column) and with the rotation pre-processing step (right column).

5 Applications

5.1 Curve Reconstruction and Generation

Curve reconstruction typically refers to the process of using a set of observed sample points providing only partial information about a curve, to estimate the full closed curve. The predictive capabilities of the aforementioned multiple-output GP model can be used to accomplish this task for closed curves. In particular, we know that this estimated closed curve will be consistent thanks to the periodic constraint. To demonstrate curve reconstruction, we consider two practical scenarios.

First, suppose that we have one set of curves with sample points characterizing its full underlying shape, and this is augmented with another set of curves where sample points are only available in a particular region, e.g., under a cluster sampling scheme. A simple example of this is shown in Figure 8, where the first camel is sampled in clusters only around its top part, and the other two camels are sampled more evenly along its true boundary. This scenario occurs, for example, in images where an object boundary is partially-observed, perhaps due to the presence of another object which is obstructing it.

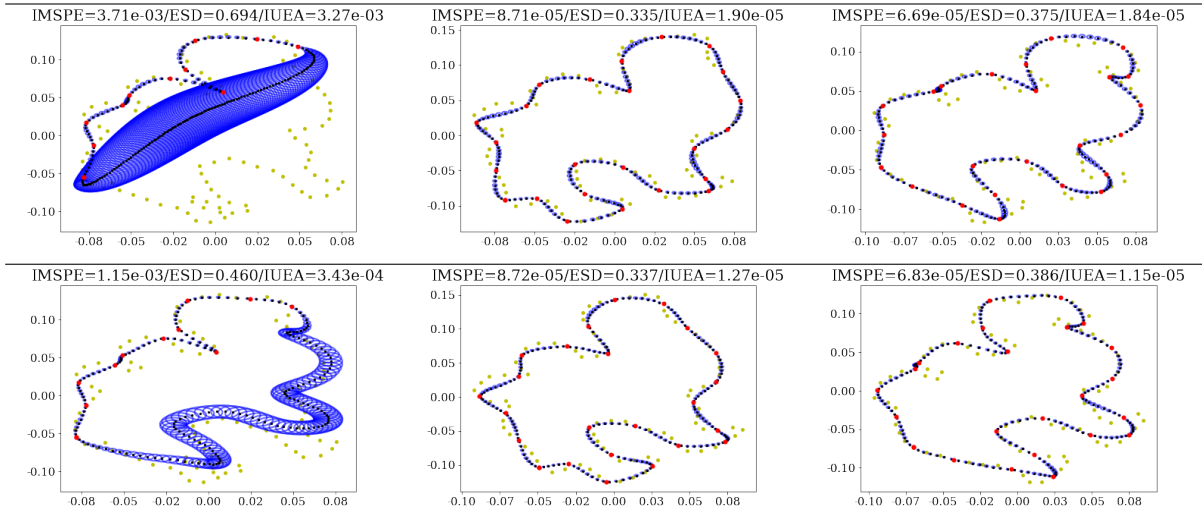


Figure 8: **Curve reconstruction with uncertainty quantification via multiple-output GP modeling.** Three camel curves from MPEG-7, modeled using separate multiple-output GPs for each curve (top) and a jointly fit multiple-output GP (bottom). The first bone is cluster sampled at 13 points, while the other two bones are sampled equally-spaced at 25 points.

Separating independent multiple-output GP models for each curve results in an inadequate estimate for the first curve. However, the jointly fit multiple-output GP model can exploit similarity across curves to improve estimation of the camel’s legs with increased predictive uncertainty than in the region where points were observed.

Second, consider a scenario where limited observations are available, i.e., observed points are sparsely sampled, for three leaves from the Flavia dataset (Wu et al., 2007). A goal of analyzing multiple curves may be to obtain a representative shape, for instance, in data such as Flavia where leaves come from multiple classes. A standard representative shape summary from elastic shape analysis is the Karcher mean, found by minimizing the sum of squared distances within the elastic shape space. This involves shape registration, which can perform unfavorably in sparse sampling regimes and/or in the presence of noise.

Even if leaves are randomly resampled to 101 points, the Karcher mean estimates are quite sensitive to sparse samples, sampling schemes, and noisy samples. An alternative is to fit a multiple-output GP to the collection of curves, and then take pointwise averages of the predictive means across curves. This ensures that the representative curve is also closed, and modeling between-curve dependence learns the relationships across curves at varying parameter values. Note that this pointwise predictive mean characterizes the representative shape of these leaves much better than the alternatives presented here. Increasing the number of observed sample points (panels (b) and (c)) can mitigate some of these issues accompanying the raw and resampled Karcher means, where pointwise predictive means look more similar to the Karcher mean estimated using the full 101 points; however, the presence of noise can exacerbate issues, as shown in panel (d), while the GP enhanced Karcher mean is robust to noise. The bottom of the figure shows Gromov-Wasserstein (GW) distances (see Supplementary Materials I), which can be used to quantify “how closely aligned” two point clouds are. Here, each curve is compared to the Karcher mean computed using all 101 points; note that the pointwise GP predictive mean outperforms

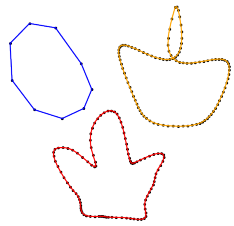
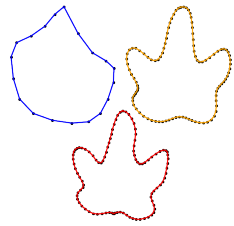
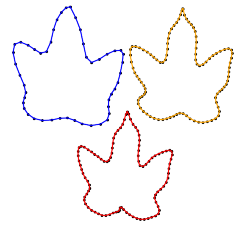
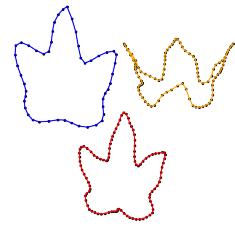
	(a) No noise, 10	(b) No noise, 20	(c) No noise, 50	(d) Noise, 50
				
(I)	3.38×10^{-2}	2.39×10^{-2}	1.41×10^{-2}	1.43×10^{-2}
(II)	1.90×10^{-2}	1.35×10^{-2}	9.32×10^{-3}	2.62×10^{-2}
(III)	4.86×10^{-3}	1.30×10^{-2}	2.03×10^{-3}	2.37×10^{-3}

Figure 9: **Comparison of mean shapes from GP modeling and Karcher mean computation.** Panel (a) shows Karcher means from the 10 observed sample points shown in the top panel (blue, row labeled (I)) and interpolative re-sampling to 101 observed sample points (orange, (II)), and pointwise predictive mean across curves from GP fitting (red, (III)). Panels (b) and (c) show these estimates for 20 and 50 observed sample points, respectively, and panel (d) shows these estimates for 50 sample points observed with Gaussian noise (standard deviation 0.007). Table entries at bottom show the Gromov-Wasserstein distance between corresponding colored curve and the Karcher mean computed using 101 dense samples.

other alternatives here.

5.2 Elastic Shape Registration

An important task for statistical modeling of curves is shape registration, where the goal is to place curves in pointwise correspondence with each other by applying various shape-preserving transformations. Elastic shape registration usually performs best when curves are densely sampled along the entire curve (details are found in the Supplementary Materials G). In addition, computational implementations of registration typically require curves to be sampled at the same number of points. Fitting the multiple-output GP model, followed by re-sampling using the predictive mean, can allow for shape registration in a wide variety of situations, e.g., if the original data is of low quality, as seen in Figure 9. Thus, our goal is the following: given two curves, perhaps sampled at a different number of points and/or perturbed by noise, can we satisfactorily register one (deemed the target) to the other (the source)?

We propose fitting observed sample points to our MOGP model to obtain closed curve estimates. Predictive means for both target and source curves can be sampled at an equal, large number of points to ensure the fitted curves are densely sampled. Then, these dense sample points from the fitted curve estimates can be registered to each other. This is a more robust way to perform elastic registration compared to using the originally sampled points, which can be observed at different resolutions and potentially with noise.

Figure 10 shows two lizard curves, one sampled at 15 points and the other at 50 points, both equally-spaced and perturbed by bivariate Gaussian noise. We can fit a multiple-output GP to exploit the structural similarity between the two lizards, obtaining predictive mean curves. These are then densely sampled at the same number of points for registration.

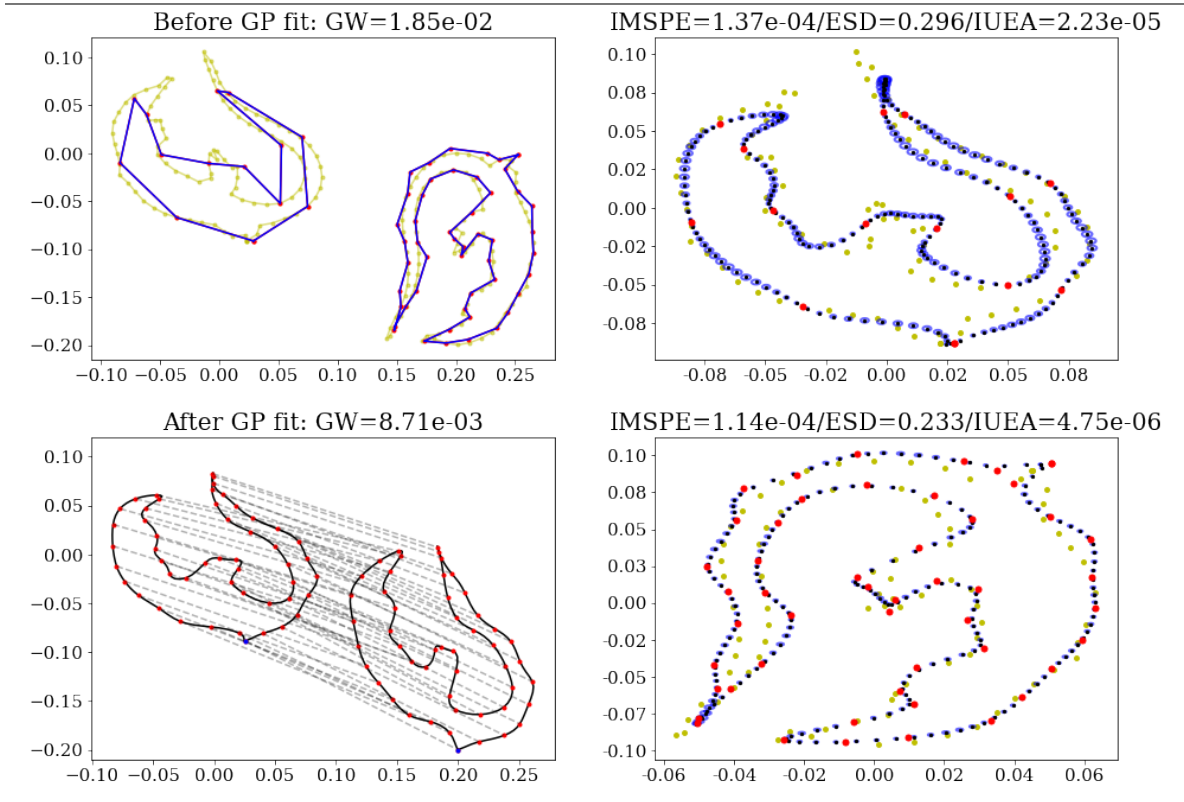


Figure 10: **Elastic registration of curves observed at different number of sample points with noise.** (Top left) Two lizard curves from MPEG-7, sampled equally-spaced at 15 (left) and 50 (right) points (red), perturbed pointwise by uncorrelated, bivariate normal noise with standard deviation 0.005. (Right panel) Estimates from jointly fit multiple-output GP. (Bottom left) Correspondence (black dashed lines) between camels induced by elastic registration based on predicted mean curves, sampled at 100 points each with red points marking every 4 points. The blue point in the bottom two panels are the aligned “starting points” of the curves.

Our proposed method is a natural way of performing elastic registration in a way which bridges the gap from different and potentially small numbers of sparse sampling points to a equal number of dense samples along fitted mean curves, without arbitrary re-sampling. The GW metric confirms this: using the observed sample points, the GW distance is 1.85×10^{-2} ; however, the point clouds formed by elastic registration of predictive means from GP fitting have a reduced GW distance of 8.71×10^{-3} . Model-based group mean is preferred to Karcher mean when only irregular samples are available.

5.3 Landmark Selection

The third application discussed is landmark selection. Unlike shape registration, where we densely re-sample points from the fitted model, here we consider two different approaches to identify a small set of landmarks (i.e., observed sample points) on each curve that provides a compressed representation of its corresponding densely-sampled original curve. Theorem 2 guarantees the consistency of the model when the curves are densely sampled.

However, dense samples are not always practical for modeling or computing purposes. Thus, selecting a small set of observed sample points to adequately represent the original curve is important. For instance, given an image, boundary estimation procedures produce curves which are often very densely sampled. If one wishes to apply landmark-based (Dryden and Mardia, 2016) or curve-based (Srivastava et al., 2011) shape analysis methods to these curves, a principled approach to subsampling to a small set of observed points is a useful step. This can be done either (i) sequentially, or (ii) simultaneously, using uncertainty estimates obtained by our proposed GP model.

Some landmark detection methods have been developed for general manifolds. Prematilake and Ellingson (2018) considers arc-length and curvature parameterizations to evaluate approximation error of the piecewise-linear approximations, driven by selected landmarks. Strait et al. (2019a) considers further a Bayesian model which quantifies the discrepancy under the elastic framework, obtaining uncertainty quantification for landmarks. These methods consider the task of simultaneous landmarking: starting with a densely sampled curve, a smaller set of landmarks is proposed, and the piecewise-linear curve through these points is compared to the original curve. This is different from a sequential approach, e.g., Gao et al. (2019), where given a sample of observed points (on an open manifold), the next landmark is chosen sequentially to minimize predictive variance under a fitted model. In general, landmarking has also been studied for images (particularly of a certain type), often relying on domain knowledge or supervised models, which incorporate subject-matter expert annotations (Chen et al., 2014; Tie and Guan, 2013; Domijan and Wilson, 2005).

The proposed multiple-output GP model can handle both formulations of the landmarking problem. To perform simultaneous landmarking, we start with a collection of multiple curves (often assumed to be densely sampled), with the goal of estimating p landmarks for each curve. A simple procedure is as follows: (1) repeatedly generate p random parameter values, denote this \mathbf{s} , common to all curves; (2) fit the multiple-output GP model to the Euclidean coordinates corresponding to \mathbf{s} ; (3) compare model fits to the original, densely sampled set of points using performance metrics (Supplementary Materials I). For instance, we may want the landmark set \mathbf{s} which minimizes IMSPE, aggregated over curves. Similar to Strait et al. (2019a), if an estimate \hat{p} of the number of landmarks is desired, the chosen performance metric can be evaluated over a set of pre-specified values of p . Then, \hat{p} is selected either qualitatively, as the smallest value where the minimum IMSPE begins to stabilize, or quantitatively using, e.g., the gap statistic (Tibshirani et al., 2001).

Figure 11 demonstrates this simultaneous landmarking procedure on three Flavia leaves, assumed to be densely sampled. For $p \in \{3, \dots, 20\}$ landmarks, 1000 sets of landmarks \mathbf{s} are randomly sampled without replacement from the densely-sampled curves, and the joint multiple-output GP model is fit. Each fit is evaluated based on average IMSPE and IUEA across the three curves; the random landmark configuration which minimizes these quantities for each p is shown in the top left panel of the figure. For IMSPE, this value begins to stabilize around $\hat{p} = 10$ landmarks, whereas the IUEA plot has a more steady decrease. The other panels show the joint fit for the optimally chosen $\hat{p} = 10$ landmarks under the IMSPE criteria; note that the fitted curves here provide a fairly adequate approximation of the original curves, supporting our preference for observed sample points to be equally-spaced along the curve domain. We note that this simple procedure is computationally expensive; one could integrate this within a Bayesian model-based approach, e.g., Strait et al. (2019a,b), for improved fitting, but we leave this as future work.

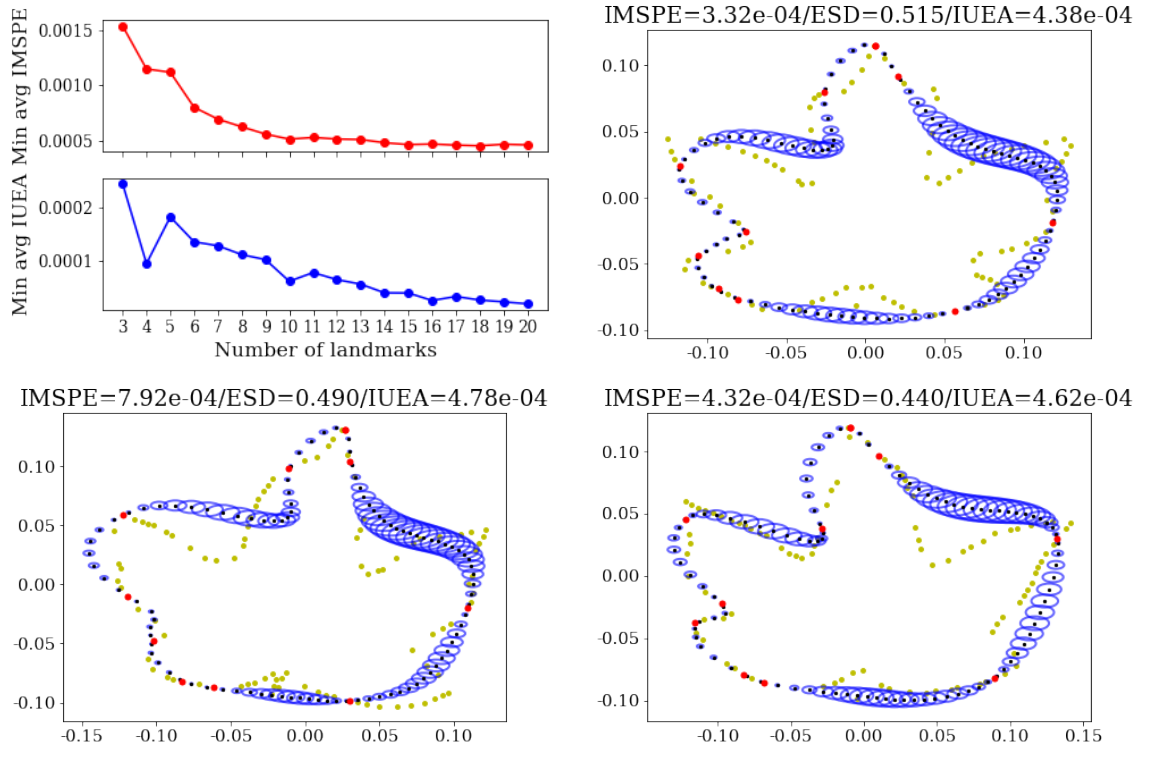


Figure 11: **Simultaneous landmarking for multiple curves.** Three leaves from the same class of the Flavia dataset (top right and bottom panels), modeled using jointly fit multiple-output GP based on $\hat{p} = 10$ landmarks. The top left panel shows the minimum average IMSPE (red) and IUEA (blue) as a function of p landmarks

We also outline a sequential procedure for landmarking, inspired by Gao et al. (2019), as follows: (1) fit a GP (either separate single-output or multiple-output) to the curve(s); (2) obtain the estimated 2×2 -dimensional prediction variance matrix for both coordinates of a single curve, $\tilde{\Sigma}_p(s^*)$, with each coordinate’s predictive variances $\tilde{\sigma}_{p1}(s^*)$, $\tilde{\sigma}_{p2}(s^*)$ on the diagonal; (3) set the next landmark s_{p+1} as:

$$s_{p+1} = \operatorname{argmax}_{s^* \in \mathcal{D}} (\lambda \tilde{\sigma}_{p1}(s^*) + (1 - \lambda) \tilde{\sigma}_{p2}(s^*)) . \quad (7)$$

The value $\lambda \in [0, 1]$ controls how much weight is attributed to the predictive variance of the first coordinate, and is pre-specified by the user. A standard choice is to set $\lambda = 0.5$ for equal weighting.

Figure 12 shows a comparison of the sequential landmarking procedure to select the next landmark on the same three Flavia leaves. In this scenario, leaves are sampled at 7 random points along the true curve, and a GP is fit under the single-output, separate curve-level multiple-output, and joint multiple-output kernel formulations. Once fit, the next landmark is identified as the point on the true curve which solves Equation (7). Note how this landmark varies between different choices of model fits. In the first two panels, the landmark is in different locations across curves due to the assumption of between-curve independence. While uncertainty is reduced by going to separate multiple-output models, landmark locations do not shift much. However, the joint multiple-output model fits tend

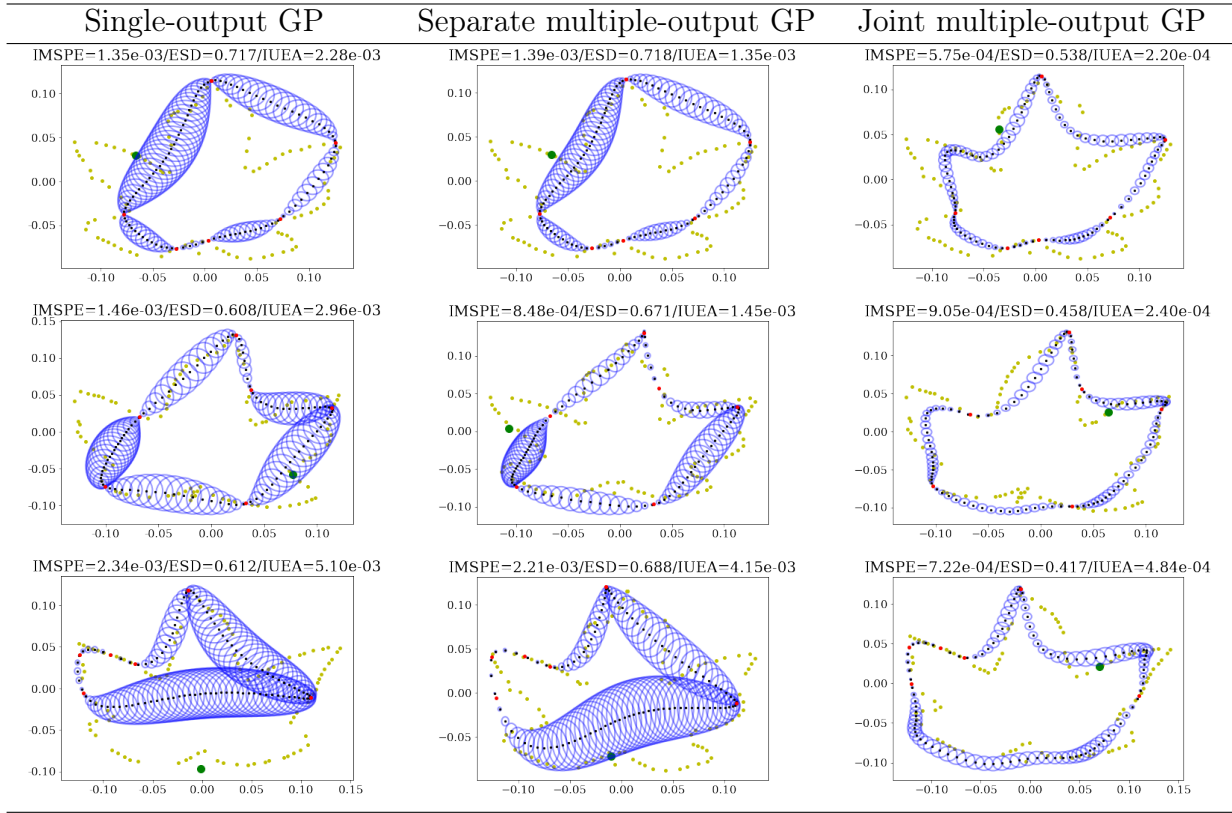


Figure 12: **Iterative landmarking comparison between single-output, separate multiple-output, and joint multiple-output GP models for multiple curves.** Three leaves from the same class of the Flavia dataset, modeled using single-output GPs (left column), separate multiple-output GPs for each curve (middle column) and a jointly fit multiple-output GP (right column). Each leaf is observed at 7 sample points, randomly selected from the true curve. The next landmark suggested by the strategy (7), is illustrated by the green point on the true curve.

to more closely resemble the three leaves because of the structural similarity. As a result, the next landmark is selected to be near the top of all three curves. Landmarking based on the joint model can be more efficient, as information is shared across curves in model fitting.

Note that both sequential and simultaneous landmark selection appear to prefer landmark configurations that resemble a uniform sampling. In a sense, the uniform sampling is not only the default choice in a dense sampling to ensure both model consistency (c.f., Theorem 2) and arc-length parameterization consistency (c.f., Theorem 3), but also provides a natural candidate for landmark selection based on GP models.

5.4 Modeling Sub-populations

The multiple-output GP model for closed curves can be extended to model multiple sub-populations, which is useful if there are substantial shape differences between them. In this setting, each curve is supplemented with a class label to indicate sub-population membership. One may want closed curve fits which respect these labels, such that curves within

the same class are more similar than those from different classes. In the context of our multiple-output model, this means that full information sharing across the entire collection of curves may not be appropriate. Instead, the kernel can be modified to encourage enhanced within-class information sharing. This can be achieved by further stacking of kernels, leading to a dependence structure with an additional level for class labels. This stacking can be performed naturally under the assumption of separable kernels.

Formally, suppose that for the curve $j = 1, \dots, J$, we observe n_j sample points with corresponding arc-length parameter values, $(s_i^{(j)}, \mathbf{y}_i^{(j)})$, assumed to be drawn from the underlying curve $\mathbf{f}^{(j)} = (f_1^{(j)}, f_2^{(j)})$. We also assume that each curve has class label $L^{(j)} \in \{1, \dots, r\}$, i.e., curves are drawn from r sub-populations, with $r \leq J$. A simple way to specify a kernel which accounts for class labels is by assuming the full kernel has a separable structure, i.e., $K = k \otimes k_D \otimes k_C \otimes k_G$, with elements $\text{Cov}\left(f_d^{(j)}(s), f_{d'}^{(j')}(s')\right) = k(s, s')k_D(d, d')k_C(j, j')k_G(g, g')$, where k , k_D , and k_C are specified as in Section 4, and k_G is the group-level kernel that compares the class labels $L^{(j)} = g$ and $L^{(j')} = g'$ for the curves j and j' . As in previous cases, a simple choice is to use the intrinsic coregionalization model, defining a $r \times r$ -dimensional coregionalization matrix G such that $G_{g,g'} = k_G(g, g')$, constrained to be symmetric and positive semi-definite.

Figure 13 shows two classes of leaf curves from the Flavia dataset, with each class containing 16 leaves. Suppose these curves are observed using 10 equally-spaced points, so that shape information is fairly minimal. Column (a) shows model fits when pooling all 32 curves together, i.e., ignoring class label information. In this case, the simply-shaped leaves of the second class are estimated to have more complex shape, as jointly modeling all curves borrows information across both classes. Since the first class has leaves with more curvature, some of these features are transferred to the fitting of leaves in the second class. This is reflected in the mean IMSPE values for curves within this class.

However, by fitting a multiple-output GP model using the above kernel specification with coregionalization class label kernel, the model uses the sub-population information to produce predicted mean curves which more closely resemble the initial curves that observed points were sampled from. In addition, curves within a class which differ somewhat from other curves sharing the same label display a higher predictive variance in regions between points. We note that, as pre-processing for curves being modeled as drawn from multiple sub-populations, observed sample points are optimally rotated to the first curve within its class.

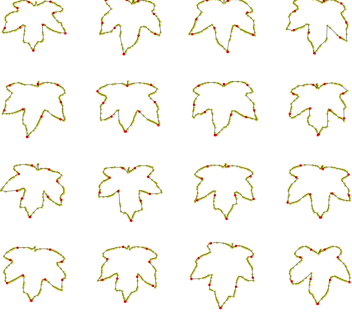
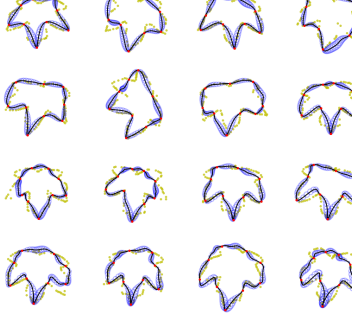

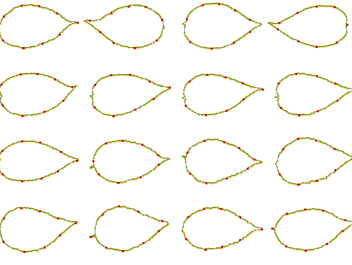
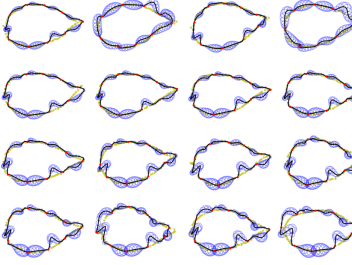
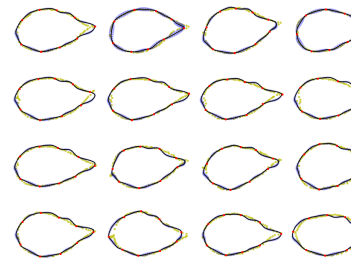
	(a)	(b)
		
Mean IMSPE	6.62×10^{-4}	5.41×10^{-4}
Mean ESD	0.474	0.423
Mean IUEA	2.15×10^{-4}	5.33×10^{-5}
		
Mean IMSPE	6.01×10^{-4}	3.41×10^{-4}
Mean ESD	0.407	0.249
Mean IUEA	5.32×10^{-4}	5.11×10^{-5}

Figure 13: **Comparing multiple-output GP fits for clustered curves.** Sixteen leaves each from two sub-populations (corresponding to the two rows) of the Flavia dataset, modeled using (a) multiple-output GP with no class label kernel, and (b) multiple-output GP with coregionalization class label kernel. Each leaf is observed at 10 sample points, selected from the true curve as shown in the top panel. Averaged IMSPE, ESD, and IUEA (see Supplementary Materials I) across curves within each class is reported.

6 Conclusion

In this paper, we formulate an approach for fitting closed curves using the nonparametric multiple-output GP model. The GP model provides a generative way for sampling and re-sampling of fitted closed curves, allowing certain sampling assumptions (e.g., the presence of dense samples) to be relaxed for applications of curve-based shape analysis methods such as registration, reconstruction, and simultaneous/sequential landmark selection.

We discuss theoretical and practical difficulties presented by GP fitting of closed curves, first addressing these challenges for a single curve through the introduction of a multi-level dependence structure. This structure includes a periodic stationary covariance kernel on the input space, combined with a coregionalization kernel for the coordinate functions of a curve. We also extend this dependence structure to jointly model multiple curves through an additional coregionalization kernel to capture between-curve dependence. This allows model fitting to exploit the structural similarity of curves, improving predictions while reducing uncertainty.

Since closed curves belong to a family of closed manifolds with different topology than open curves or univariate functional data, our modeling approach is a continuation of existing efforts to incorporate topological information into statistical methods (Luo and Strait, 2019). We note that our multi-curve GP model extends naturally to closed curves (and their shapes) embedded in higher dimensional spaces (rather than \mathbb{R}^2), although non-trivial generalizations are needed for modeling hypersurfaces with dimension greater than 1.

Our probabilistic modeling framework can lead to several directions for future work. As mentioned above, we can consider a wider variety of coregionalization kernel construction other than product kernels (e.g., additive and convolution); specifically, we can consider local kernels of specific forms, with the sub-population kernel as a special case. Within the modeling of curve sub-populations, one can modify the curve label kernel to incorporate continuous metrics which quantify curve similarity. In addition, it would be interesting to explore how geometric (smoothness) information could assist the choice of kernels, as this could allow our proposed model to be extended to incorporate both topological (Nigmetov and Morozov, 2022; Luo et al., 2021) and geometrical information (Solomon et al., 2021; Chowdhury and Needham, 2021) in real-world applications. Another natural extension is a fully Bayesian version of this GP model, which can incorporate prior curvature and/or shape class information (e.g., Lu et al. (2017)). The main challenges with this are the choice of constrained prior and posterior computation and approximation, as pointed out by Yang et al. (2016) in the functional data analysis context.

From the perspective of computational efficiency, we plan to extend landmark selection as a dimension reduction tool for curve fitting. The sparse GP (Luo et al., 2022) can use geometrically-informed landmarks as pseudo-inputs. Unlike the current model, the sparse GP incorporates the Nyström approximation, which requires careful selection of pseudo-inputs with respect to the local features expressed by the closed curve and boundaries. Combined with the geometric information incorporated within, the sparse GP model can be used not only as a tool of selecting important landmarks for curve representation, but also as an optimal subsampling tool for data compression. Uncertainty quantification obtained by our model-based GP approach can be applied to numerous other problems within statistical shape analysis. In particular, many applications within elastic shape analysis do not account for the uncertainty quantification associated with curve fitting in a systematic way, as the necessary computation of the elastic shape metric treats shapes as deterministic objects.

Acknowledgments: To the best of our knowledge, we claim no conflict of interest with this manuscript. The code to produce all figures and experiments can be found at <http://www.github.com/hrluo>. HL thanks the Scalable Solvers group for support during this project, as well as Didong Li for discussion and data analysis suggestions. We both thank Sebastian A. Kurtek for early discussions on previously related literature within shape analysis, along with Samir Chowdhury for a series of presentations and discussions which directed us to Gromov-Wasserstein metrics.

References

- Ahdesmäki, M., H. Lähdesmäki, R. Pearson, H. Huttunen, and O. Yli-Harja (2005). Robust detection of periodic time series measured from biological systems. *BMC bioinformatics* 6(1), 1–18.
- Aronszajn, N. (1950). Theory of reproducing kernels. *Transactions of the American mathematical society* 68(3), 337–404.
- Bai, X., X. Yang, L. J. Latecki, W. Liu, and Z. Tu (2009). Learning context-sensitive shape similarity by graph transduction. *IEEE Transactions on Pattern Analysis and Machine Intelligence* 32(5), 861–874.
- Basak, S., S. Petit, J. Bect, and E. Vazquez (2021). Numerical issues in maximum likelihood parameter estimation for gaussian process interpolation. *arXiv preprint arXiv:2101.09747*.
- Bonilla, E. V., K. Chai, and C. Williams (2007). Multi-task gaussian process prediction. *Advances in neural information processing systems* 20.
- Bookstein, F. L. (1986). Size and shape spaces for landmark data in two dimensions. *Statistical Science* 1(2), 181–222.
- Borovitskiy, V., A. Terenin, P. Mostowsky, et al. (2020). Matérn gaussian processes on riemannian manifolds. *Advances in Neural Information Processing Systems* 33, 12426–12437.
- Boyd, S., S. P. Boyd, and L. Vandenberghe (2004). *Convex optimization*. Cambridge university press.
- Braun, M. L. (2006). Accurate error bounds for the eigenvalues of the kernel matrix. *The Journal of Machine Learning Research* 7, 2303–2328.
- Chapelle, O., V. Vapnik, O. Bousquet, and S. Mukherjee (2002). Choosing multiple parameters for support vector machines. *Machine learning* 46(1), 131–159.
- Chen, C., W. Xie, J. Franke, P. Grutzner, L.-P. Nolte, and G. Zheng (2014). Automatic x-ray landmark detection and shape segmentation via data-driven joint estimation of image displacements. *Medical Image Analysis* 18(3), 487–499.
- Cheng, W., I. L. Dryden, and X. Huang (2016). Bayesian Registration of Functions and Curves. *Bayesian Analysis* 11(2), 447 – 475.
- Cho, Y. and L. Saul (2009). Kernel methods for deep learning. *Advances in neural information processing systems* 22.
- Chowdhury, S. and F. Mémoli (2019). The gromov–wasserstein distance between networks and stable network invariants. *Information and Inference: A Journal of the IMA* 8(4), 757–787.

- Chowdhury, S. and T. Needham (2021). Generalized spectral clustering via gromov-wasserstein learning. In *International Conference on Artificial Intelligence and Statistics*, pp. 712–720. PMLR.
- Cramér, H. and M. R. Leadbetter (2013). *Stationary and related stochastic processes: Sample function properties and their applications*. Courier Corporation.
- Cressie, N. (2015). *Statistics for spatial data*. John Wiley & Sons.
- Dareiotis, K. and B. Gess (2019). Supremum estimates for degenerate, quasilinear stochastic partial differential equations. In *Annales de l’Institut Henri Poincaré, Probabilités et Statistiques*, Volume 55, pp. 1765–1796. Institut Henri Poincaré.
- Domijan, K. and S. Wilson (2005). A bayesian method for automatic landmark detection in segmented images. In *Proceedings of the 22nd International Conference on Machine Learning*.
- Dryden, I. L. and K. V. Mardia (2016). *Statistical shape analysis: with applications in R*, Volume 995. John Wiley & Sons.
- Duvenaud, D. (2014). *Automatic model construction with Gaussian processes*. Ph. D. thesis, University of Cambridge.
- Eubank, R. L. and P. Speckman (1990). Curve fitting by polynomial-trigonometric regression. *Biometrika* 77(1), 1–9.
- Falconer, K. (2004). *Fractal geometry: mathematical foundations and applications*. John Wiley & Sons.
- Fisher, N. I. (1995). *Statistical analysis of circular data*. cambridge university press.
- Fisher, N. I., T. Lewis, and B. J. Embleton (1993). *Statistical analysis of spherical data*. Cambridge university press.
- Fisher, R. A. (1929). Tests of significance in harmonic analysis. *Proceedings of the Royal Society of London. Series A, Containing Papers of a Mathematical and Physical Character* 125(796), 54–59.
- Flamary, R., N. Courty, A. Gramfort, M. Z. Alaya, A. Boissunon, S. Chambon, L. Chapel, A. Corenflos, K. Fatras, N. Fournier, L. Gautheron, N. T. Gayraud, H. Janati, A. Rakotomamonjy, I. Redko, A. Rolet, A. Schutz, V. Seguy, D. J. Sutherland, R. Tavenard, A. Tong, and T. Vayer (2021). Pot: Python optimal transport. *Journal of Machine Learning Research* 22(78), 1–8.
- Gao, T., S. Z. Kovalsky, and I. Daubechies (2019). Gaussian process landmarking on manifolds. *SIAM Journal on Mathematics of Data Science* 1(1), 208–236.
- Gasser, T. and A. Kneip (1995). Searching for structure in curve samples. *Journal of the American Statistical Association* 90(432), 1179–1188.

- Gelfand, A. E., A. Kottas, and S. N. MacEachern (2005). Bayesian nonparametric spatial modeling with dirichlet process mixing. *Journal of the American Statistical Association* 100(471), 1021–1035.
- Gramacy, R. B. (2020). *Surrogates: Gaussian process modeling, design, and optimization for the applied sciences*. Chapman and Hall/CRC. OCLC: 1120696204.
- Greven, S. and F. Scheipl (2017). A general framework for functional regression modelling. *Statistical Modelling* 17(1-2), 1–35.
- Huang, W., K. A. Gallivan, A. Srivastava, and P.-A. Absil (2016). Riemannian optimization for registration of curves in elastic shape analysis. *Journal of Mathematical Imaging and Vision* 54, 320–343.
- Joshi, S. and A. Srivastava (2009). Intrinsic Bayesian active contours for extraction of object boundaries in images. *International Journal of Computer Vision* 81(3), 331–355.
- Kass, M., A. Witkin, and D. Terzopoulos (1988). Snakes: active contour models. *International Journal of Computer Vision* 1, 321–331.
- Kendall, D. G. (1984). Shape manifolds, Procrustean metrics, and complex projective spaces. *Bulletin of the London Mathematical Society* 16(2), 81–121.
- Kim, H. J., N. Adluru, H. Suri, B. C. Vemuri, S. C. Johnson, and V. Singh (2017). Riemannian nonlinear mixed effects models: Analyzing longitudinal deformations in neuroimaging. In *Proceedings of the IEEE Conference on Computer Vision and Pattern Recognition*, pp. 2540–2549.
- Klassen, E., A. Srivastava, W. Mio, and S. Joshi (2004, 04). Analysis of planar shapes using geodesic paths on shape spaces. *IEEE transactions on pattern analysis and machine intelligence* 26, 372–83.
- Koepf, P. and F. Pfaff (2021). Consistency of gaussian process regression in metric spaces. *Journal of Machine Learning Research* 22(244), 1–27.
- Kurtek, S., A. Srivastava, E. Klassen, and Z. Ding (2012). Statistical modeling of curves using shapes and related features. *Journal of the American Statistical Association* 107(499), 1152–1165.
- Lu, Y., R. Herbei, and S. Kurtek (2017). Bayesian registration of functions with a gaussian process prior. *Journal of Computational and Graphical Statistics* 26(4), 894–904.
- Luo, H., Y. Cho, J. W. Demmel, X. S. Li, and Y. Liu (2022). Hybrid models for mixed variables in bayesian optimization. *arXiv:2204.10975*, 1–57.
- Luo, H., J. W. Demmel, Y. Cho, X. S. Li, and Y. Liu (2021). Non-smooth bayesian optimization in tuning problems. *arXiv preprint arXiv:2109.07563*.
- Luo, H., J. Kim, A. Patania, and M. Vejdemo-Johansson (2021). Topological transfer learning for time series and motion data. *The IEEE International Conference on Big Data (IEEE BigData 2021)*, 1–6.

- Luo, H., S. MacEachern, and M. Peruggia (2020). Asymptotics of lower dimensional zero-density regions. *arXiv:2006.02568*, 1–27.
- Luo, H., G. Nattino, and M. T. Pratola (2022). Sparse additive gaussian process regression. *Journal of Machine Learning Research* 23(61), 1–34.
- Luo, H., A. Patania, J. Kim, and M. Vejdemo-Johansson (2021). Generalized penalty for circular coordinate representation. *Foundations of Data Science*, 1–37.
- Luo, H. and J. Strait (2019). Combining geometric and topological information in image segmentation. *The IEEE International Conference on Big Data (IEEE BigData 2021)*.
- MacKay, D. J. et al. (1998). Introduction to gaussian processes. *NATO ASI series F computer and systems sciences* 168, 133–166.
- Matthews, A. G. d. G., M. van der Wilk, T. Nickson, K. Fujii, A. Boukouvalas, P. León-Villagrà, Z. Ghahramani, and J. Hensman (2017, apr). GPflow: A Gaussian process library using TensorFlow. *Journal of Machine Learning Research* 18(40), 1–6.
- Minh, H. Q., P. Niyogi, and Y. Yao (2006). Mercer’s theorem, feature maps, and smoothing. In *International Conference on Computational Learning Theory*, pp. 154–168. Springer.
- Nigmatov, A. and D. Morozov (2022). Topological optimization with big steps. *arXiv preprint arXiv:2203.16748*.
- Olsen, N. L., B. Markussen, and L. L. Raket (2018). Simultaneous inference for misaligned multivariate functional data. *Journal of the Royal Statistical Society: Series C (Applied Statistics)* 67(5), 1147–1176.
- Paciorek, C. J. (2003). *Nonstationary Gaussian processes for regression and spatial modelling*. Ph. D. thesis, Carnegie Mellon University.
- Plutowski, M., S. Sakata, and H. White (1993). Cross-validation estimates imse. *Advances in neural information processing systems* 6.
- Prematilake, C. and L. Ellingson (2018, May). Evaluation and prediction of polygon approximations of planar contours for shape analysis. *Journal of Applied Statistics* 45(7), 1227–1246.
- Quinn, B. G. (1989). Estimating the number of terms in a sinusoidal regression. *Journal of time series analysis* 10(1), 71–75.
- Risser, M. D. (2016). Nonstationary spatial modeling, with emphasis on process convolution and covariate-driven approaches. *arXiv preprint arXiv:1610.02447*.
- Rodríguez, A., D. B. Dunson, and A. E. Gelfand (2009). Bayesian nonparametric functional data analysis through density estimation. *Biometrika* 96(1), 149–162.
- Shi, J. Q. and T. Choi (2011). *Gaussian process regression analysis for functional data*. CRC Press.

- Siegel, A. F. (1980). Testing for periodicity in a time series. *Journal of the American Statistical Association* 75(370), 345–348.
- Snelson, E. and Z. Ghahramani (2006). Sparse gaussian processes using pseudo-inputs. In *Advances in neural information processing systems*.
- Solomon, E., A. Wagner, and P. Bendich (2021). From geometry to topology: Inverse theorems for distributed persistence. *arXiv preprint arXiv:2101.12288*.
- Srivastava, A., E. Klassen, S. Joshi, and I. Jermyn (2011). Shape analysis of elastic curves in Euclidean spaces. *IEEE Transactions on Pattern Analysis and Machine Intelligence* 33(7).
- Srivastava, A. and E. P. Klassen (2016). *Functional and shape data analysis*, Volume 1. Springer.
- Steyer, L., A. Stöcker, and S. Greven (2021). Elastic analysis of irregularly or sparsely sampled curves. *arXiv preprint arXiv:2104.11039*.
- Stöcker, A. and S. Greven (2021). Functional additive regression on shape and form manifolds of planar curves. *arXiv preprint arXiv:2109.02624*.
- Strait, J., O. Chkrebtii, and S. Kurtek (2019a). Automatic detection and uncertainty quantification of landmarks on elastic curves. *Journal of the American Statistical Association* 114, 1002–1017.
- Strait, J., O. Chkrebtii, and S. Kurtek (2019b). Parallel tempering strategies for model-based landmark detection on shapes. *Communications in Statistics - Simulation and Computation* 51(4), 1415–1435.
- Tibshirani, R., G. Walther, and T. Hastie (2001). Estimating the number of clusters in a data set via the gap statistic. *Journal of the Royal Statistical Society: Series B (Statistical Methodology)* 63(2), 411–423.
- Tie, Y. and L. Guan (2013). Automatic landmark point detection and tracking for human facial expressions. *EURASIP Journal on Image and Video Processing* 8.
- Tucker, J. D. (2021). *fdasrf*. Python module version 2.2.9.
- Tucker, J. D., W. Wu, and A. Srivastava (2013). Generative models for functional data using phase and amplitude separation. *Computational Statistics & Data Analysis* 61, 50–66.
- van der Wilk, M., V. Dutordoir, S. John, A. Artemev, V. Adam, and J. Hensman (2020). A framework for interdomain and multioutput Gaussian processes. *arXiv:2003.01115*.
- Wang, B. and J. Q. Shi (2014). Generalized gaussian process regression model for non-gaussian functional data. *Journal of the American Statistical Association* 109(507), 1123–1133.

- Wang, J.-L., J.-M. Chiou, and H.-G. Müller (2016). Functional data analysis. *Annual Review of Statistics and Its Application* 3, 257–295.
- Wassermann, D., M. Toews, M. Niethammer, and W. Wells (2014). Probabilistic diffeomorphic registration: Representing uncertainty. In *International Workshop on Biomedical Image Registration*, pp. 72–82. Springer.
- Williams, C. K. and C. E. Rasmussen (2006). *Gaussian processes for machine learning*, Volume 2. MIT press Cambridge, MA.
- Wu, S. G., F. S. Bao, E. Y. Xu, Y.-X. Wang, Y.-F. Chang, and Q.-L. Xiang (2007). A leaf recognition algorithm for plant classification using probabilistic neural network. In *2007 IEEE international symposium on signal processing and information technology*, pp. 11–16. IEEE.
- Yang, J., H. Zhu, T. Choi, and D. D. Cox (2016). Smoothing and mean–covariance estimation of functional data with a bayesian hierarchical model. *Bayesian Analysis* 11(3), 649–670.
- Zang, X., S. Kurtek, O. Chkrebti, and J. D. Tucker (2020). Elastic k-means clustering of functional data for posterior exploration, with an application to inference on acute respiratory infection dynamics. *arXiv:2011.12397v1*, 1–33.
- Zaytsev, A., E. Romanenkova, and D. Ermilov (2018). Interpolation error of gaussian process regression for misspecified case. In *Conformal and Probabilistic Prediction and Applications*, pp. 83–95. PMLR.
- Zeng, P., J. Qing Shi, and W.-S. Kim (2019). Simultaneous registration and clustering for multidimensional functional data. *Journal of Computational and Graphical Statistics* 28(4), 943–953.

SUPPLEMENTARY MATERIAL

A Shape and Parameterizations

As mentioned in Section 2, there is a distinction between closed curves and their shapes, and a few notes are necessary with respect to the distinction. First, when modeling a single closed curve, we can use the phrase "closed curve" and "shape" interchangeably, noting that the observed closed curve is a representative element of its shape equivalence class. The distinction is more important when considering multiple curves: discussion of shape within this paper implies that closed curves (i.e., their estimates from GP fitting) have been registered under the elastic shape metric.

In this paper, closed curves are functions $\mathbf{f} : \mathcal{S}^1 \rightarrow \mathbb{R}^2$. Shape can be defined in numerous ways, depending on how curves are represented. For this paper, we follow the definition ascribed by elastic shape analysis literature (Srivastava et al., 2011), where shape is a mathematical representation of a curve which is invariant to translation, scale, rotation, and curve parameterization. This is an extension of landmark shape spaces (Kendall, 1984;

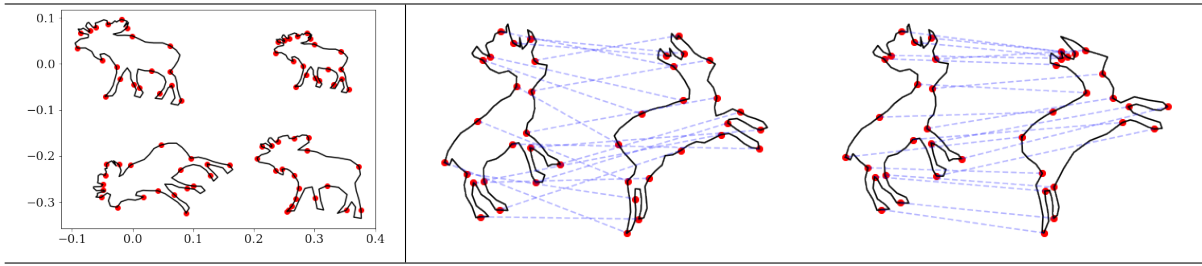


Figure 14: **Shapes and comparison of parameterizations.** (Left) Four deer curves (in black) from MPEG-7 with equivalent shape, as they only differ by a translation, scaling, rotation, and/or re-parameterization. (Middle and right) Two deer curves, comparing correspondence induced by arc-length parameterizations (middle) to that induced by elastic parameterizations (right). Red points are in correspondence across curves (sampled with respect to their parameterizations), with dashed blue lines showing the points in correspondence.

Bookstein, 1986; Dryden and Mardia, 2016), which do not consider parameterization, as shape is represented by finite point sets. More formally, the shape of curve \mathbf{f} is an equivalence class, containing all curves which only differ by one of the above shape-preserving transformations. The elastic shape space \mathcal{S} is the set of all such equivalence classes. The left panel of Figure 14 shows an example of four closed curves (representing deer from the MPEG-7 dataset) which belong to the same equivalence class (i.e., have identical shape) in \mathcal{S} .

The middle panel show two different deer curves parameterized by arc-length. Note that the legs are not correctly matched to each other, as these features occur at different arc-length parameter values along the two curves. The right panel shows correspondences between the same two deer from the middle panel when curve parameterizations are induced by the elastic metric. Note that this appropriately matches the aforementioned legs, and in general results in a more apt comparison between the two deer.

B Arc-length Parameterization Algorithms

In the setting where closed curves are densely sampled, the arc-length parameter is approximated well by inscribed polygons; however, in general, the approximation error cannot be ignored. In this section, we present two algorithms to map between observed sample points on closed curves and their corresponding arc-length parameter values. We also provide theoretical error bounds for these algorithms.

Note that these algorithms compute quantities with respect to an underlying curve. For simulations, this can be the (known) true curve, but in practice, this is assumed to be with respect to the piecewise-linear curve constructed from connecting observed sample points. This simple choice is appropriate, as one goal of the model is to estimate the underlying curve, and the ordering of observed sample points reflects the curve’s sampling scheme.

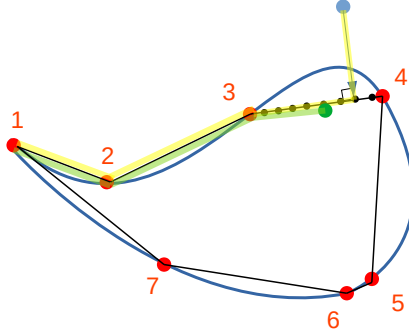


Figure 15: **Arc-length parameterization algorithms.** An illustration with 7 red points (their orderings are displayed) sampled from the underlying blue solid curve; point 1 is the starting point, followed by the points 2, 3, \dots , 7. The black piecewise linear curve approximation constructed by connecting these points. Black segments are obtained from connecting red points, and serves as a reference. Black points are sampled from black segments to compute the closest distance from an external point to the curve.

B.1 Enclosing Curves

In Figure 15, we can see that Algorithm 1 converts the blue point's x - and y -coordinates (which is not necessarily on the black curve) into its corresponding arc-length parameter value represented by yellow shaded segment, and is numerically computed by identifying a densely "over-sampled" black point on the linear approximating curve. In this procedure, there are two approximations: the first is in joining observed points by line segments for curve approximation (Step 5 in Algorithm 1), i.e., yellow highlighted and black segments in Figure 15. This is intrinsic to the curve. The second approximation comes from computing "point-to-segment" distance by dense sampling on the line segment between two consecutive points (Steps 7 to 9 in Algorithm 1), i.e., N_b black dots on the segments between points 3 and 4 in Figure 15. This depends on the extrinsic metric defined in \mathbb{R}^2 . Algorithm 2 converts the green point with arc-length parameter value represented by green shaded segment into x - and y -coordinates (always on the black curve) with reference to the linear approximating curve. In this procedure, only the intrinsic curve approximation is used, and not the extrinsic metric in \mathbb{R}^2 .

As stated in our algorithm, we enclose the input sample points by replicating the first column to the last column. This is crucial in estimating the total arc-length. If we do not enclose the input sample points, then we are treating the sample points as being drawn from an open curve. As a result, any points located between the observed last and first points in the sample will be mapped to either the first or the last point. This results in an error as large as the length of the segment between last and first point. In addition, the presented algorithms behave less consistently, due to dependence on the first and last sampled points. This error is generally small when we have dense sample points (which is the usual setup in elastic shape analysis), yet when there are finitely many sample points, this enclosing step becomes more crucial.

We wrap up this section by presenting the algorithm complexity for conversion algo-

Algorithm 1: `xy_to_arc_param_single`: converts an observed sample point's (x, y) -coordinates (from a closed curve) into its arc-length parameter value

Data: `osamp` ($2 \times (n + 1)$ matrix, columns are (x, y) -coordinates for n ordered sample points from a closed curve in \mathbb{R}^2 , where final column is same as first column)

Input: `xy_coord` ((x, y) -coordinates for point which arc-length parameter is desired)

Result: `arc_param` (arc-length parameter value for the target point `xy_coord`)

```

1 (1) Generate "over-sampled" piecewise linear curve ospl
   ( $2 \times ((n + 1)(N_b + 1) - N_b)$  matrix) by linearly interpolating  $N_b$  points between
   each consecutive pair of points contained in osamp to find the closest point to the
   target point;
2   begin
3     set  $N_b$  (e.g.,  $N_b = 19$  is sufficient);
      /* final iteration connects final point to starting point */
4     for  $i \leftarrow 1$  to  $n$  do
5       ospl[:,  $i \cdot (N_b + 1) - N_b$ ] = osamp[:,  $i$ ]; /* direction to move to next
        sample point along segment */
6       vecd = osamp[:,  $i + 1$ ] - osamp[:,  $i$ ];
7       for  $j \leftarrow 1$  to  $N_b$  do
8         ospl[:,  $i \cdot (N_b + 1) - N_b + j$ ]  $\leftarrow$  ospl[:,  $i \cdot (N_b + 1) - N_b + j - 1$ ] +  $\frac{j}{N_b + 1}$ vecd;
9       end
10    end
11    ospl[:,  $(n + 1)(N_b + 1) - N_b$ ] = osamp[:,  $n + 1$ ];
12  end
13 (2) Compute the closest distance between xy_coord and each point in ospl;
14 (3) Identify the point cl_ospl along "over-sampled" piecewise linear curve that is
    closest to xy_coord;
15 (4) Identify immediately preceding sample point prev_sp to xy_coord along ospl
    and compute arc-length of ospl up to prev_sp;
16 return arc_param = arc-length from starting point to prev_sp + arc-length
    between prev_sp and cl_ospl

```

rithms. Although the complexity is straightforward from construction, we want to point out that these are linear in n , the number of sample points.

Proposition 1. *The complexity of Algorithm 1 is $O(N_b \cdot n)$. The complexity of Algorithm 2 is $O(n)$.*

B.2 Curve Length Estimation

As the number of observed sample points increases, one obtains an increasingly accurate estimate of the underlying curve's arc-length. Recall that we use y_{i1}, y_{i2} for the x and y -coordinates of observed sample point i , as in (1), and we identify the $(n + 1)$ -th point with the first point, i.e., $y_{n+1,d} := y_{1d}$ for $d = 1, 2$, based on our closed curve assumption.

Algorithm 2: `arc_to_xy_param_single`: converts an arc-length parameter along a closed curve into (x, y) -coordinates

Data: `osamp` ($2 \times (n + 1)$ matrix, columns are (x, y) -coordinates for n ordered sample points from a closed curve in \mathbb{R}^2 , where final column is same as first column)

Input: `arc_param` (arc-length parameter value for which (x, y) -coordinates are desired)

Result: `xy_coord` ((x, y) -coordinates in \mathbb{R}^2 corresponding to `arc_param`)

```

1 (1) Compute arc-length parameter values based on osamp;
2   begin
3     res[1] = 0 ;
4     for  $i \leftarrow 2$  to  $n + 1$  do
5       |   res[i]  $\leftarrow$  res[i - 1] + |osamp[:, i] - osamp[:, i - 1]|;
6     end
7   end
8 (2) Identify sample point with arc-length parameter just preceding (or equal to)
    arc_param;
9   dst = |arc_param - res|;
10  previ = index of sample point prev_sp preceding or equal to arc_param based
    on dst;
11 (3) Linear interpolation based on arc-length distance to prev_sp;
12  begin
13    prev_dst = |arc_param - res[previ]|;
14    interval_dst = res[previ + 1] - res[previ];
15    rat =  $\frac{\text{prev\_dst}}{\text{interval\_dst}}$ ;
16    xy_coord = osamp[:, previ] + rat (osamp[:, previ + 1] - osamp[:, previ]);
17  end
18 return xy_coord.

```

Then, for underlying curve $\mathbf{f} = (f_1, f_2)$, its total arc-length is given by $\ell(\mathbf{f}) := \int_{\mathbf{f}} ds = \int_{(x,y) \in \mathbf{f}} \sqrt{\left(\frac{df_1}{ds}\right)^2 + \left(\frac{df_2}{ds}\right)^2} ds$. Thus, the absolute error for estimation of its total arc-length is bounded from above by:

$$\begin{aligned}
\Delta &:= \sum_{i=1}^n \left| \int_{s \in [s_i, s_{i+1}]} \sqrt{\left(\frac{df_1}{ds}\right)^2 + \left(\frac{df_2}{ds}\right)^2} ds - \sqrt{(y_{i+1,1} - y_{i1})^2 + (y_{i+1,2} - y_{i2})^2} \right| \\
&\leq \sum_{i=1}^n \left| (s_{i+1} - s_i) \max_{s \in [s_i, s_{i+1}]} \sqrt{\left(\frac{df_1}{ds}\right)^2 + \left(\frac{df_2}{ds}\right)^2} - \sqrt{(y_{i+1,1} - y_{i1})^2 + (y_{i+1,2} - y_{i2})^2} \right|,
\end{aligned}$$

where $f_1(s), f_2(s)$ are univariate x, y -coordinates functions with shared parameter s . As in the main text, we assume this parameter is the arc-length parameter, although other choices are allowed. This bound depends on the curvature of $\mathbf{f}(s)$ and the maximal difference between sample point coordinates. The total error bound above can be decomposed into

error bounds which depend on consecutive ordered sample points (y_{i1}, y_{i2}) and $(y_{i+1,1}, y_{i+1,2})$ with arc-length parameters s_i, s_{i+1} :

$$\begin{aligned}\tilde{\Delta}_i &:= \left| (s_{i+1} - s_i) \max_{s \in [s_i, s_{i+1}]} \sqrt{\left(\frac{df_1}{ds}\right)^2 + \left(\frac{df_2}{ds}\right)^2} - \sqrt{(y_{i+1,1} - y_{i1})^2 + (y_{i+1,2} - y_{i2})^2} \right| \\ &\leq (s_{i+1} - s_i) \max_{s \in [s_i, s_{i+1}]} \sqrt{\left(\frac{df_1}{ds}\right)^2 + \left(\frac{df_2}{ds}\right)^2} - \sqrt{(y_{i+1,1} - y_{i1})^2 + (y_{i+1,2} - y_{i2})^2} \\ &\leq (s_{i+1} - s_i) \max_{s \in [s_i, s_{i+1}]} \left(\left| \frac{df_1}{ds} \right| + \left| \frac{df_2}{ds} \right| \right) - \sqrt{(y_{i+1,1} - y_{i1})^2 + (y_{i+1,2} - y_{i2})^2}.\end{aligned}$$

The absolute value can be removed because the shortest distance between two points is achieved by a straight line segment connecting them when in \mathbb{R}^2 . The last inequality comes from the fact that $\sqrt{a+b} \leq \sqrt{a} + \sqrt{b}$ for positive a, b . The following result ensures that under a reasonable sampling scheme, our algorithm gives a consistent estimate of the total curve length.

Theorem 3. *Suppose that we sampled the points (y_{i1}, y_{i2}) from the underlying curve defined by (f_1, f_2) , and both coordinate functions are first-order Lipschitz with constants $C_x, C_y > 0$. The total estimation error $\Delta = \sum_{i=1}^n \tilde{\Delta}_i$ converges to 0 as $\max_i \|s_{i+1} - s_i\| \rightarrow 0$.*

Proof. We know that both coordinate functions are Lipschitz with constants $C_x, C_y > 0$, i.e., $\|\frac{df_1}{ds}(s) - \frac{df_1}{ds}(s')\| \leq C_x \|s - s'\|$, $\|\frac{df_2}{ds}(s) - \frac{df_2}{ds}(s')\| \leq C_y \|s - s'\|$. Then, the pointwise error, as defined above, is bounded by:

$$\begin{aligned}\tilde{\Delta}_i &\leq (C_x + C_y) \cdot (s_{i+1} - s_i) - \sqrt{(y_{i+1,1} - y_{i1})^2 + (y_{i+1,2} - y_{i2})^2} \\ &= (C_x + C_y) \cdot (s_{i+1} - s_i) - \sqrt{(f_1(s_{i+1}) - f_1(s_i))^2 + (f_2(s_{i+1}) - f_2(s_i))^2}.\end{aligned}\quad (8)$$

The equality follows from the additional assumption that points are sampled from the underlying curve, though our algorithm works without this assumption. From this bound, we immediately see that when $\max_i \|s_{i+1} - s_i\| \rightarrow 0$, the first summand in (8) converges to 0 uniformly. The second summand also converges to 0 uniformly due to the Lipschitz assumption. Using the dominated convergence theorem, we know the sum $\Delta = \sum_i^n \tilde{\Delta}_i$ also converges to 0. \square

This error bound $\tilde{\Delta}_i$ suggests a uniform sampling over the arc-length space tends to minimize the overall estimation error $\Delta = \sum_i \tilde{\Delta}_i$, since both terms in the definition of Δ are minimized by a uniform equally-spaced sampling over a curve of fixed length, given a fixed number of sample points. A cluster sampling would maximize both terms at least for one i_0 and break the condition that $\max_i \|s_{i+1} - s_i\| \rightarrow 0$ in the above consistency result, which supports Algorithm 1. The following corollary follows from Algorithm 2.

Corollary 1. *Under the same assumption of Theorem 3, a point **on** the underlying curve of arc-length $s_0 > 0$ is mapped to the segment between two points $(y_{n_0+1,1}, y_{n_0+1,2})$ and*

$(y_{n_0,1}, y_{n_0,2})$ such that:

$$\sum_{i=0}^{n_0} \sqrt{(y_{i+1,1} - y_{i1})^2 + (y_{i+1,2} - y_{i2})^2} \leq s_0 \leq \sum_{i=0}^{n_0+1} \sqrt{(y_{i+1,1} - y_{i1})^2 + (y_{i+1,2} - y_{i2})^2},$$

with accumulative error bounded from above by $\sum_{i=0}^{n_0+1} \tilde{\Delta}_i$.

Algorithm 2 may suffer from accumulative error, but it also enjoys the consistency result expressed in terms of error bounds above, when $\max_i \|s_{i+1} - s_i\| \rightarrow 0$.

C Gaussian Processes

We next review basic, single-output Gaussian process regression models. Assume we observe n input-output pairs, (s_i, y_i) , where $s_i \in \mathcal{D}$ and $y_i \in \mathbb{R}$ (hence "single-output"). A GP regression model relates input variable s_i to corresponding output with noise y_i through an unknown target function f :

$$y_i = f(s_i) + \epsilon_i, \quad \epsilon_i \stackrel{\text{iid}}{\sim} \mathcal{N}_1(0, \sigma_\epsilon^2), \quad i = 1, \dots, n, \quad (9)$$

where ϵ_i represents observation error. In vector notation, we have $\mathbf{y} = f(\mathbf{s}) + \boldsymbol{\epsilon}$, where $\mathbf{y} = (y_1, \dots, y_n)^T$, $\mathbf{s} = (s_1, \dots, s_n)^T$, $f(\mathbf{s}) = (f(s_1), \dots, f(s_n))^T$, and $\boldsymbol{\epsilon} \sim \mathcal{N}_n(\mathbf{0}_n, \sigma_\epsilon^2 \mathbf{I}_n)$. The primary goal is to estimate the underlying f , which is not assumed to have any particular shape or parametric form.

Following the convention by Snelson and Ghahramani (2006), we assume a priori that the mean vector $f(\mathbf{s})$ is a realization of a zero mean Gaussian process, $f \sim \mathcal{GP}(0, k)$, for covariance kernel $k(\cdot, \cdot) : \mathcal{D} \times \mathcal{D} \rightarrow \mathbb{R}$. The kernel $k(s_i, s_j) = \text{Cov}(f(s_i), f(s_j))$ models local correlations of the unknown target function f , which in turn ultimately controls its smoothness of f . Samples from this Gaussian process implies the following joint multivariate normal distribution, $f(\mathbf{s}) \sim \mathcal{N}_n(\mathbf{0}_n, \mathbf{K}_n)$, where $\mathbf{K}_n = [k(s_i, s_j)]_{i,j=1}^n$ is the n -dimensional covariance matrix. Gaussian processes are fully specified by the mean and covariance functions, and typically we set the mean function to be identically zero a priori, reflecting lack of knowledge.

The form of covariance kernel k is often chosen from a specific family of kernels (e.g., radial basis function family, Matern family) which has its own set of hyperparameters, and the choice of kernel can vary for different applications. For instance, consider the radial basis function (RBF) kernel: $k_{(\sigma^2, \rho)}(s_i, s_j) = \sigma^2 \exp\{-\|s_i - s_j\|^2 / (2\rho^2)\}$. This kernel has two hyperparameters: σ^2 scales the covariance appropriately with output variance, and ρ is the length scale, which controls how quickly the dependence decays.

We take the frequentist approach in GP model fitting, typically performed by optimizing its log marginal likelihood to estimate kernel hyperparameters. Bayesian approaches to fitting also exist, but are not investigated in the current work (Gramacy, 2020). Once the hyperparameters of the covariance kernel have been estimated, predictions can be elicited at a new input s^* with the mean and variance below:

$$\begin{aligned} \tilde{\mu}(s^*) &= \mathbf{K}(s^*, \mathbf{s}) (\mathbf{K}_n + \sigma_\epsilon^2 \mathbf{I}_n)^{-1} \mathbf{y} \\ \tilde{\sigma}^2(s^*) &= k(s^*, s^*) - \mathbf{K}(s^*, \mathbf{s}) (\mathbf{K}_n + \sigma_\epsilon^2 \mathbf{I}_n)^{-1} \mathbf{K}(s^*, \mathbf{s})^\top, \end{aligned} \quad (10)$$

where $\mathbf{K}(s^*, \mathbf{s}) = [k(s^*, s_i)]_{i=1}^n$ is a n -dimensional vector of kernel evaluations between the new input for prediction and observed inputs. The predictive mean $\tilde{\mu}(s^*)$ is a kernel-weighted combination of observed outputs, and its predictive uncertainty is given by $\tilde{\sigma}^2(s^*)$.

D Proof of Theorem 1

For $r := \|s_i - s_j\| \in (0, \ell/2)$, we first factor out σ^2 of the stationary periodic covariance kernel $k_{(\sigma^2, \rho, \tau)}(s_i, s_j) = k_{(\sigma^2, \rho, \tau)}(0, r)$, defined by Equation (3). Then, consider the Taylor expansion of this function at $r = 0$:

$$\begin{aligned} \exp\left(-\frac{1}{\rho} \sin^2\left(\frac{r}{\tau/\pi}\right)\right) &= 1 - \frac{\pi^2}{\rho\tau^2} \cdot r^2 + \frac{1}{4} \left(\frac{2\pi^4}{\rho^2\tau^4} + \frac{4\pi^4}{3\rho\tau^4}\right) \cdot r^4 - O(r^6) \\ \Rightarrow \exp\left(-\frac{1}{\rho} \sin^2\left(\frac{r}{\tau/\pi}\right)\right) &\geq 1 - \frac{\pi^2}{\rho\tau^2} \cdot r^2 \\ \Rightarrow \exp\left(-\frac{1}{\rho} \sin^2\left(\frac{r}{\tau/\pi}\right)\right) &\leq 1 + \frac{1}{4} \left(\frac{2\pi^4}{\rho^2\tau^4} + \frac{4\pi^4}{3\rho\tau^4}\right) \cdot r^4. \end{aligned}$$

Therefore, using the fact that $r = \|s_1 - s_2\| < \ell/2$, we obtain the lower bound:

$$k_{(\sigma^2, \rho, \tau)}(s_i, s_j) \geq \sigma^2 \left(1 - \frac{\pi^2}{\rho\tau^2} \cdot \|s_i - s_j\|^2\right) \geq \sigma^2 \left(1 - \frac{\pi^2 \ell^2}{4\rho\tau^2}\right), \quad (11)$$

Similarly, we get the following upper bound:

$$k_{(\sigma^2, \rho, \tau)}(s_i, s_j) \leq \sigma^2 \left(1 + \frac{1}{4} \left(\frac{2\pi^4}{\rho^2\tau^4} + \frac{4\pi^4}{3\rho\tau^4}\right) \cdot \|s_i - s_j\|^4\right) \leq \sigma^2 \left(1 + \frac{1}{64} \left(\frac{2\pi^4}{\rho^2\tau^4} + \frac{4\pi^4}{3\rho\tau^4}\right) \cdot \ell^4\right). \quad (12)$$

We compare the periodic kernel to its non-periodic counterpart. One way to do this is by minimizing the difference between the upper bound (12) and the lower bound (11), so that the periodic kernel behaves like its non-periodic counterpart (i.e., squared exponential), such that a pair of points at maximal distance $\ell/2$ can attain a small kernel value, and any oscillations of kernel values are dampened within a period. If the difference between upper and lower bounds is large, then there may exist many oscillations within a period, as shown in Figure 16. On the other hand, we also observe a trade-off between the periodic parameter τ and the length scale parameter ρ in the upper bound. For the upper bound, when we assume that $\tau = \delta\ell$ for some $\delta \approx 1$, the upper bound (12) reduces to $\sigma^2 \left(1 + \frac{1}{64} \left(\frac{2\pi^4}{\rho^2\delta^4} + \frac{4\pi^4}{3\rho\delta^4}\right)\right)$.

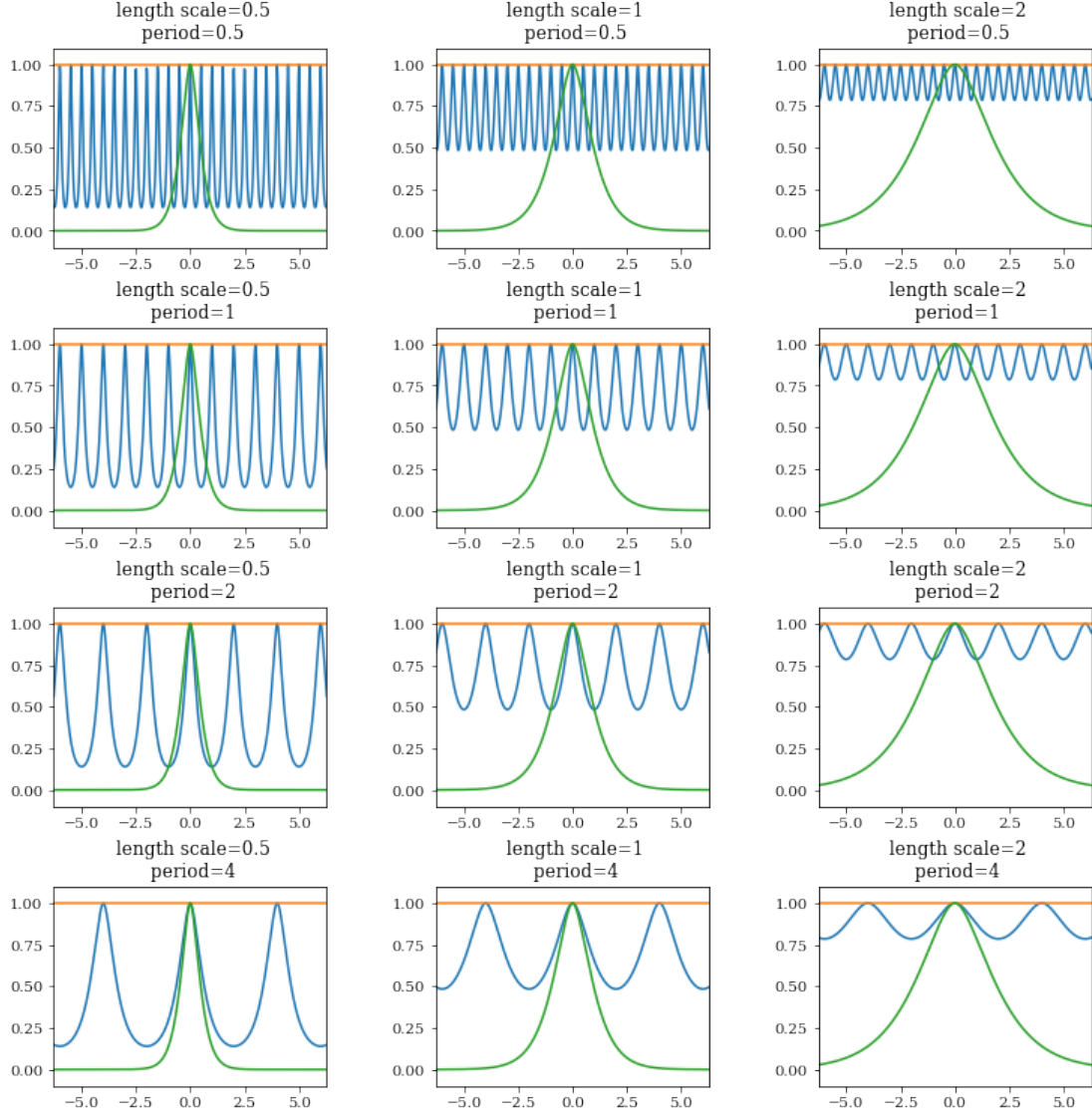


Figure 16: **Trade-off between length scale and period kernel hyperparameters.** Comparison of kernel evaluations for different length scale and period hyperparameters (where applicable). The periodic Matern 3/2 kernel is in blue, the Matern 3/2 kernel in green, and the value 1 in orange (i.e., the value of a degenerate kernel with 0 or infinite period). The x -axis is the arc-length r along the curve between two points $s_i, s_j \in \mathcal{D}$ and the y -axis is kernel evaluation $k(0, r)$.

E Proof of Theorem 2

Recall that the domain we consider for closed curves is $\mathcal{D} = \mathcal{S}^1$. When endowed with an intrinsic metric, \mathcal{S}^1 is separable, since we can find points corresponding to rational degrees dense on \mathcal{S}^1 . It is also σ -compact, since \mathcal{S}^1 can be represented as a countable union of closed balls centered at these points with rational degrees. Any parameterization s that is isometric to the arc-length metric on \mathcal{S}^1 will also induce a separable and σ -compact metric space \mathcal{D} . This verifies the conditions of Theorem 3 in Koepernik and Pfaff (2021) and leads to the L_2 convergence results of Statement (i).

Next, we verify the conditions of Theorem 8 in Koepernik and Pfaff (2021). In conjunction with Proposition 7 in the same paper, it suffices to verify that the Minkowski dimension of \mathcal{D} is finite and the kernel $k_{(\sigma^2, \rho, \tau)}$ is locally Lipschitz. The finiteness of Minkowski dimension follows either by definition (e.g., Definition 3.1 in Falconer (2004), see also Luo et al. (2020) for a discussion for lower dimensional embedded curves) or by direct computation of the Dudley integral using the natural covering of \mathcal{S}^1 consisting of balls centered at rational degrees. Lipschitz continuity follows from the bounds, specifically (12), in the proof of Theorem 1. The periodic kernel defined in (3) is continuous for fixed, estimated finite, non-zero hyperparameters (σ^2, ρ, τ) . Then, by Proposition 7 in Koepernik and Pfaff (2021), we know that the Dudley integral $J(C, \|\cdot\|) = \int_0^\infty \sqrt{\log N(C, \varepsilon, \|\cdot\|)} d\varepsilon < \infty$ for all compact sets in $\mathcal{D} = \mathcal{S}^1$. Inside the integral, the integrand $N(C, \varepsilon, \|\cdot\|)$ is the covering number of C using ε -balls w.r.t. the metric $\|\cdot\|$ defined by the periodic kernel $k_{(\sigma^2, \rho, \tau)}$.

Using Condition (i) of Proposition 4 and Theorem 8 (Koepernik and Pfaff, 2021), with all of its assumptions verified above, we can claim that the posterior GP is continuous for all sample sizes as in Statement (ii). Furthermore, let $\prod_n = \mathcal{GP}(\hat{f}_{i,n}, k_n)$ be the product measure based on mean coordinate function $\hat{f}_{i,n}$ (for $i = 1, 2$) and covariance function k_n (i.e., (10)) under a sample of size n . As an element defined on a functional space, this product measure satisfies $\prod_n(U) \xrightarrow{L_1} 1$ for every open neighborhood U of the continuous f_1, f_2 . However, this aspect of consistency is less relevant in our discussion of sampling.

F Non-stationary Kernels

One can also consider non-stationary kernels in GP fitting to model non-smoothness in greater detail (Risser, 2016; Paciorek, 2003). Non-stationary kernels relax the stationarity constraint and increase the flexibility in kernel hyperparameter values, which can be allowed to vary along the input space. Precisely, a stationary kernel can be expressed as solely a function of the input difference, whereas a non-stationary kernel cannot be. An example of a GP fit using a non-stationary kernel is shown in Figure 17, using the arc-cosine kernel of order 0, defined in Equation (1) of Cho and Saul (2009), a popular choice within deep learning. While this does similarly allow for less smooth estimation in the region around the antennae, the slight noise perturbation significantly alters estimates of the arc-cosine kernel’s hyperparameters (which has no consideration of period), and results in a curve fit which is not closed. We remark that a non-stationary kernel does not allow an analog of the periodicity constraint for stationary kernels, so consistency (i.e., Theorem 2) cannot be guaranteed, and we cannot expect $\mathbf{f}(0) = \mathbf{f}(\ell)$ in general. This behavior does not occur as drastically for more densely sampled curves, but we have observed that periodic stationary

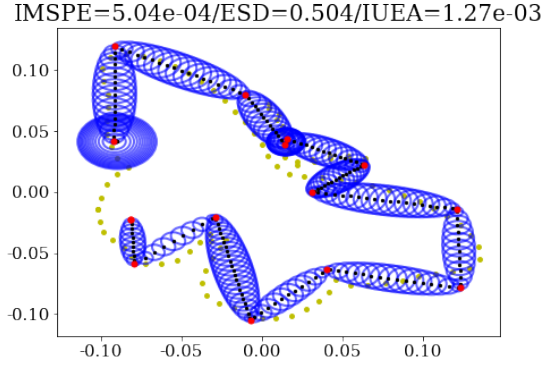


Figure 17: **Non-stationary kernel fit.** A butterfly curve from MPEG-7 sampled at 20 points, perturbed pointwise by uncorrelated bivariate normal noise with standard deviation 0.008, and modeled using separate single-output GPs under the non-stationary, non-periodic arc-cosine kernel of order 0. It is clear that the kernel produces inconsistency.

kernels are more robust in general, as shown in Figure 5.

Figure 18 shows lizard curve fits for all combinations of either sparse or dense observed sample points under either stationary (periodic Matern 3/2) or non-stationary (arc-cosine) kernels. If a sparse set of observed points are available, we recommend using a periodic stationary kernel, which guarantees consistency, shows kriging behavior, and can generally result in smoother fits. In comparison, the non-stationary kernel does appear to produce a consistent curve (unlike Figure 17), but this curve is not very smooth given the limited number of observed sample points. On the other hand, if the set of observed points is dense, we recommend either periodic stationary or non-stationary kernels, as both are able to capture finer details of the lizard curve with reduced uncertainty.

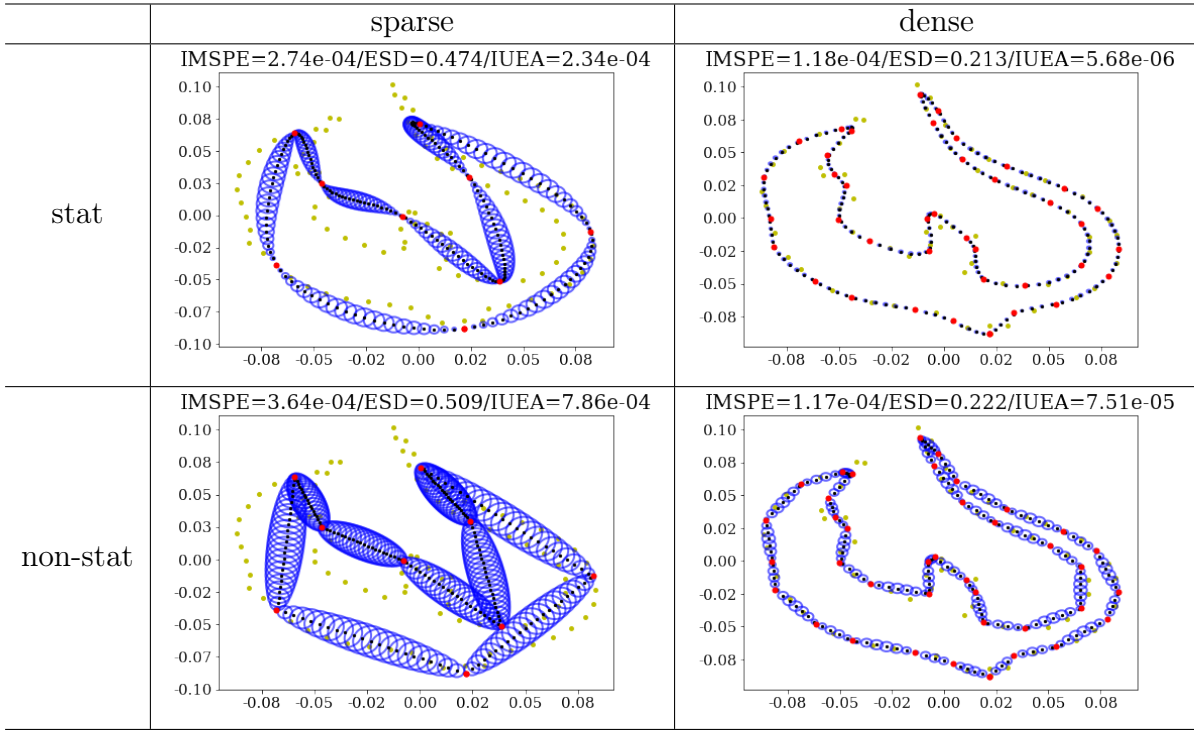


Figure 18: **Comparison of stationary and non-stationary fits by sampling scheme.** Lizard curve from MPEG-7 sampled at either 10 (sparse) or 40 (dense) observed points, and modeled using a multiple-output GP under periodic Matern 3/2 (stationary) or arc-cosine of order 0 (non-stationary) kernels.

G Elastic Shape Analysis

Elastic shape analysis (Srivastava et al., 2011; Kurtek et al., 2012) provides a set of tools for modeling the shape, viewed as equivalence classes in a shape space, of curves. An important step within elastic shape analysis is the optimal registration of curves (i.e., by rotation, translation, re-scaling, and re-parameterization) so that points on each curve corresponding to time t represents a similar feature. Elastic registration is performed by numerical optimization under what is known as the elastic metric, and assumes curves have been sampled at the same number of points. Srivastava et al. (2011) showed that the convenient square-root velocity transformation can be used to simplify calculations of the elastic metric, improving the numerical efficiency of registration.

Formally, given two closed curves $\mathbf{f}^{(j)} : \mathcal{D} \rightarrow \mathbb{R}^2$ for $j = 1, 2$, we can use the square-root velocity transformation in Equation (14) to define the *square-root velocity function (SRVF)* of the j^{th} curve $\mathbf{f}^{(j)}(s)$ by $\mathbf{q}^{(j)}(s) = F(\mathbf{f}^{(j)}(s))$. Then, pairwise elastic registration of $\mathbf{f}^{(2)}$ to $\mathbf{f}^{(1)}$ means solving the following optimization problem:

$$(O^*, \gamma^*) = \underset{O \in SO(2), \gamma \in \Gamma}{\operatorname{argmin}} \quad \|\tilde{\mathbf{q}}^{(1)} - O(\tilde{\mathbf{q}}^{(2)} \circ \gamma)\sqrt{\gamma}\|^2, \quad (13)$$

where Γ is the space of orientation-preserving re-parameterizations of curve domain \mathcal{D} , $\tilde{\mathbf{q}}^{(j)}$ denotes the re-scaling of $\mathbf{q}^{(j)}$ to unit length, \circ operates by function composition, and $\|\cdot\|$ denotes the \mathbb{L}^2 norm. In practice, this requires curves (and thus corresponding SRVFs) to be

sampled by the same number of points, and optimization proceeds by alternating between finding the optimal rotation $\tilde{O} \in SO(2)$ conditional on a fixed re-parameterization $\tilde{\gamma} \in \Gamma$, and then finding the optimal re-parameterization $\tilde{\gamma} \in \Gamma$ conditional on a fixed rotation \tilde{O} until a convergent pair is reached. Further details of this can be found in Srivastava et al. (2011). For the purpose of our discussion, it suffices to know that numerical solutions to Equation (13) rely on curves to be sampled at an equal number of points, and can be poorly conditioned for noisy curves due to the computation of SRVFs, which involves numerical differentiation.

H Pre-processing for Multiple Curves

When considering a joint multiple-output Gaussian process model with between-curve dependence, we recommend pre-processing prior to fitting, as illustrated by Figure 7. In particular, we recommend the following:

1. *Centering*: This translates curves to have its center of mass at the origin in Euclidean space. Empirically, this step does not affect the quality of the model, but assists in visualization and exploratory analysis.
2. *Scaling*: This places curves on the same scale by multiplying by a factor inversely proportional to its estimated total length based on observed sample points. This step affects the absolute values of model parameter estimates.
3. *Rotational and seed alignment*: Since the multiple-output model borrows information across Euclidean coordinates within a fixed curve, it is important to ensure that these dependencies are fairly consistent across curves. Rotating curves to match a pre-specified template as best as possible is one way to achieve this. Within this process, it is also necessary to identify similar "starting points" (referred to as "seeds") across curves in the vector of observed sample points. This can be performed simultaneously with rotational alignment.

More formally, let $\mathbf{Y}^{(j)}$ be observed sample points from curve j . Its centroid can be computed as $\bar{\mathbf{y}}^{(j)} = (\bar{y}_1^{(j)}, \bar{y}_2^{(j)})$, where $\bar{y}_d^{(j)} = \frac{1}{n_j} \sum_{i=1}^{n_j} y_{id}^{(j)}$ is the average over coordinate $d \in \{1, 2\}$. Then, the transformation $\mathbf{Y}^{(j)} \mapsto \mathbf{Y}^{(j)} - \bar{\mathbf{y}}^{(j)}$ shifts the sample points to have centroid at the origin in Euclidean space. Zero centering standardizes all sample points from the various curves to have common centroid. In landmark shape analysis (Kendall, 1984; Dryden and Mardia, 2016), this step is one way to impose translation invariance, a required first step in representing point sets within a shape space.

Standardizing the scale of observed sample points is crucial, and is also a necessary step for imposing scale invariance in landmark shape analysis. With respect to GP model fitting, we remarked in Section 3.2 that for closed curves, a periodic kernel with period close to the true arc-length of the underlying curve yields reasonable closed curve fits. If multiple curves are sharing the same input kernel, inverting the covariance matrix is more numerically stable if their scales are roughly the same.

To standardize the scale of observed sample points associated with curve j , we divide by the arc-length of the piecewise-linear polygon formed by connecting points in $\mathbf{Y}^{(j)}$ by straight line segments (as shown in Figure 15 and Algorithms 1, 2). Let this length be ℓ_j ;

then, the mapping $\mathbf{Y}^{(j)} \mapsto \frac{1}{\ell_j} \mathbf{Y}^{(j)}$ re-scales the total length of the segments as the edges of the polygons to be 1.

Finally, rotational alignment is often desired for both mapping to a landmark shape space as well as visualization purposes. Prior to fitting a joint multiple-output GP, we rotate curves $j \geq 2$ to best match a "canonical" template curve $j = 1$ chosen by a user. This canonical template curve does not have to be the first curve; for instance, if a well-defined "average" curve or some other pre-specified template curve is available, the sample of curves can be rotationally-aligned to this template instead. When performing rotational alignment, there is also a need to identify the "best" starting point, i.e., the observed sample point on curves $j \geq 2$ which best matches the first observed sample point on curve $j = 1$, which is known as seed alignment (Srivastava et al., 2011). We choose to perform these steps jointly through an iterative algorithm based on the square-root velocity formulation of Srivastava et al. (2011). This algorithm is analogous to that of solving (13); finding the optimal starting point is part of obtaining γ^* in the elastic registration problem, the primary difference is that there is no other re-parameterization performed here.

Let $\mathbf{Y}^{(j)}$ be observed sample points associated with curve j (perhaps zero-centered and re-scaled as above). We map $\mathbf{Y}^{(j)} \mapsto \mathbf{Q}^{(j)} = F(\mathbf{Y}^{(j)})$ using the square-root velocity transformation on the piecewise-linear curve $\beta_{\text{pw}}^{(j)}$ through points in $\mathbf{Y}^{(j)}$, i.e.:

$$F(\beta_{\text{pw}}^{(j)}(t)) \equiv \frac{\dot{\beta}_{\text{pw}}^{(j)}(t)}{|\dot{\beta}_{\text{pw}}^{(j)}(t)|}. \quad (14)$$

For curve $j > 2$, we transform $(\mathbf{Y}^{(j)})^T \mapsto O_j \pi_j ((\mathbf{Y}^{(j)}))^T$,

$$(O_j, \pi_j) = \underset{O \in SO(2), \pi \in \mathcal{P}}{\text{argmin}} \quad |\mathbf{Q}^{(1)} - O\pi(\mathbf{Q}^{(j)})|, \quad (15)$$

where O is a 2×2 rotation matrix in $SO(2)$, and π is a row-shift permutation of $\mathbf{Q}^{(j)}$ (in the set of row-shift permutations \mathcal{P}) which simply changes the "starting point" for curve j . Given a fixed row-shift permutation π , the optimal rotation is computed explicitly by singular value decomposition, i.e., $(\pi(\mathbf{Q}^{(j)}))^T \mathbf{Y}^{(1)} = V_j \Sigma_j U_j^T$ yields rotation matrix $O = U_j V_j^T$. We cycle through all possible row-shift permutations in \mathcal{P} , compute O_j , and choose the permutation π_j with rotation O_j which minimizes the energy in (15).

I Performance Metrics

To quantify the performance of model fitting and prediction, we discuss various metrics in this section. The first two compare model predictions to the ground truth. The third is a useful way of quantifying overall uncertainty, and the fourth is useful within the task of registration. Their formulation and respective merits are also discussed for reference.

I.1 IMSPE

The integrated mean squared prediction error (IMSPE) (Plutowski et al., 1993) characterizes the average discrepancy between a fitted curve and the ground truth curve. It was first

developed for density estimation:

$$\text{IMSPE}(f, \hat{f}) = \mathbb{E} \|\hat{f} - f\|_2^2 = \mathbb{E} \int_{\mathbb{R}^d} (\hat{f}(x) - f(x))^2 dx,$$

where the \hat{f} is the estimator of true univariate function f . When we integrate over the closed curve instead of \mathbb{R}^d , this can be taken as the average discrepancy between the GP mean and the corresponding ground truth closed curve. For finite sample of size n , we define the overall IMSPE between true closed curve $\mathbf{f} = (f_1, f_2)$ and fitted curve $\hat{\mathbf{f}} = (\hat{f}_1, \hat{f}_2)$ as:

$$\text{IMSPE}(\mathbf{f}, \hat{\mathbf{f}}) = \sum_{d=1}^2 \mathbb{E} \int_{S^1} (\hat{f}_d(s) - f_d(s))^2 ds \approx \frac{1}{n} \sum_{i=1}^n \sum_{d=1}^2 \left(\mathbb{E} \hat{f}_d(s_i) - f_d(s_i) \right)^2. \quad (16)$$

which simply takes the average of the IMSPEs across the separate x - and y -coordinate fits. Higher IMSPE values indicate that, on average, the points on the fitted curve are far from the ground truth curve.

I.2 ESD

The elastic shape distance (ESD), rooted in elastic shape analysis, can be used to quantify shape differences between fitted curve and ground truth curve. Given true closed curve contour \mathbf{f} and estimated contour $\hat{\mathbf{f}}$ based on a finite sample of points, with SRVFs \mathbf{q} and $\hat{\mathbf{q}}$ respectively, the elastic shape distance between the shape classes defined by respective curves, is given by:

$$\text{ESD}(\mathbf{f}, \hat{\mathbf{f}}) = \min_{O \in SO(2), \gamma \in \Gamma} \cos^{-1} \left(\langle \langle \mathbf{q}, O(\hat{\mathbf{q}} \circ \gamma) \sqrt{\hat{\gamma}} \rangle \rangle \right), \quad (17)$$

where $\langle \langle \cdot, \cdot \rangle \rangle$ is the \mathbb{L}^2 inner product and $SO(2)$ is the special orthogonal group. Note that this is analogous to solving (13), and requires numerical optimization. This distance quantifies shape differences which are invariant to translation, rotation, scale, and re-parameterization of the curves being compared. Higher ESD values indicate that the fitted curve has substantially different shape to the ground truth.

I.3 IUEA

We define the integrated uncertainty ellipsoid area (IUEA) to quantify overall uncertainty in GP model fitting. This is motivated by uncertainty ellipsoid plots throughout the manuscript, where pointwise uncertainty is depicted by ellipses along the predicted mean curve, with major and minor axes determined by pointwise standard deviations for the two coordinate functions. Similar to IMSPE, we can average over all points on the fitted curve to obtain an overall measure of uncertainty.

Formally, let $\tilde{\sigma}_1, \tilde{\sigma}_2$ represent the predictive standard deviations for fitted closed curve $\hat{\mathbf{f}} = (\hat{f}_1, \hat{f}_2)$. The following derivation is standard, but we cannot find it in the literature; thus, we present it for completeness. Note that at arc-length parameter value s , x - and

y -coordinates follow a bivariate normal distribution:

$$\begin{pmatrix} f_1(s) \\ f_2(s) \end{pmatrix} \sim \mathcal{N}_2 \left(\begin{pmatrix} \tilde{f}_1(s) \\ \tilde{f}_2(s) \end{pmatrix}, \begin{pmatrix} \tilde{\sigma}_1^2(s) & \tilde{\rho}_{12}(s) \\ \tilde{\rho}_{21}(s) & \tilde{\sigma}_2^2(s) \end{pmatrix} \right), \quad \tilde{\rho}_{12}(s) = \tilde{\rho}_{21}(s).$$

Therefore, by properties of normal distributions, we can write the event using a chi-squared quantile (with two degrees of freedom):

$$\mathbb{P} \left(\left[\begin{pmatrix} f_1(s) \\ f_2(s) \end{pmatrix} - \begin{pmatrix} \tilde{f}_1(s) \\ \tilde{f}_2(s) \end{pmatrix} \right]^T \begin{pmatrix} \tilde{\sigma}_1^2(s) & \tilde{\rho}_{12}(s) \\ \tilde{\rho}_{21}(s) & \tilde{\sigma}_2^2(s) \end{pmatrix}^{-1} \left[\begin{pmatrix} f_1(s) \\ f_2(s) \end{pmatrix} - \begin{pmatrix} \tilde{f}_1(s) \\ \tilde{f}_2(s) \end{pmatrix} \right] \leq \chi_{2,\alpha}^2 \right) = 1 - \alpha$$

From the Cholesky decomposition,

$$\begin{pmatrix} \tilde{\sigma}_1^2(s) & \tilde{\rho}_{12}(s) \\ \tilde{\rho}_{21}(s) & \tilde{\sigma}_2^2(s) \end{pmatrix} = \begin{pmatrix} \tilde{\sigma}_1(s) & 0 \\ \frac{\tilde{\rho}_{21}(s)}{\tilde{\sigma}_1(s)} & \sqrt{\tilde{\sigma}_2^2(s) - \frac{\tilde{\rho}_{21}^2(s)}{\tilde{\sigma}_1^2(s)}} \end{pmatrix} \begin{pmatrix} \tilde{\sigma}_1(s) & \frac{\tilde{\rho}_{21}(s)}{\tilde{\sigma}_1(s)} \\ 0 & \sqrt{\tilde{\sigma}_2^2(s) - \frac{\tilde{\rho}_{21}^2(s)}{\tilde{\sigma}_1^2(s)}} \end{pmatrix} = \mathbf{A} \mathbf{A}^T,$$

we obtain the boundary equation for a $(1 - \alpha)\%$ confidence ellipsoid of $(f_1(s), f_2(s)) \in \mathbb{R}^2$:

$$\begin{pmatrix} \tilde{\sigma}_1(s) & 0 \\ \frac{\tilde{\rho}_{21}(s)}{\tilde{\sigma}_1(s)} & \sqrt{\tilde{\sigma}_2^2(s) - \frac{\tilde{\rho}_{21}^2(s)}{\tilde{\sigma}_1^2(s)}} \end{pmatrix}^{-1} \left[\begin{pmatrix} f_1(s) \\ f_2(s) \end{pmatrix} - \begin{pmatrix} \tilde{f}_1(s) \\ \tilde{f}_2(s) \end{pmatrix} \right] = \sqrt{\chi_{2,\alpha}^2}.$$

The volume of this ellipsoid (i.e., $\left\| \frac{1}{\sqrt{\chi_{2,\alpha}^2}} (\mathbf{A}^{-1} \mathbf{f} - \mathbf{A}^{-1} \tilde{\mathbf{f}}) \right\|_2^2 \leq 1$) can be computed as a scaled unit ball \mathcal{B}^2 in \mathbb{R}^2 ($\text{vol } \mathcal{B}^2 = \pi$) (Boyd et al., 2004):

$$\begin{aligned} \sqrt{\chi_{2,\alpha}^2} \det \begin{pmatrix} \tilde{\sigma}_1(s) & 0 \\ \frac{\tilde{\rho}_{21}(s)}{\tilde{\sigma}_1(s)} & \sqrt{\tilde{\sigma}_2^2(s) - \frac{\tilde{\rho}_{21}^2(s)}{\tilde{\sigma}_1^2(s)}} \end{pmatrix} \cdot \text{vol } \mathcal{B}^2 &= \pi \sqrt{\chi_{2,\alpha}^2} \cdot \left(\tilde{\sigma}_1(s) \sqrt{\tilde{\sigma}_2^2(s) - \frac{\tilde{\rho}_{21}^2(s)}{\tilde{\sigma}_1^2(s)}} \right) \\ &= \pi \sqrt{\chi_{2,\alpha}^2} \cdot \tilde{\sigma}_1(s) \tilde{\sigma}_2(s) \text{ when } \tilde{\rho}_{21}^2(s) = 0. \end{aligned}$$

Therefore, we define the following quantity as our metric:

$$\text{IUEA}(\hat{\mathbf{f}}) = \pi \int_{\mathcal{S}^1} \left(\tilde{\sigma}_1(s) \sqrt{\tilde{\sigma}_2^2(s) - \frac{\tilde{\rho}_{21}^2(s)}{\tilde{\sigma}_1^2(s)}} \right) ds \approx \frac{\pi}{n} \sum_{i=1}^n \left(\tilde{\sigma}_1(\bar{s}) \sqrt{\tilde{\sigma}_2^2(\bar{s}) - \frac{\tilde{\rho}_{21}^2(\bar{s})}{\tilde{\sigma}_1^2(\bar{s})}} \right), \quad (18)$$

where $\bar{s} \in \mathcal{S}^1$ is determined by the intermediate valued theorem on \mathcal{S}^1 .

Note that this only accounts for between-coordinate dependence. However, from its derivation, we can see how correlation modeling for between-curve dependence, as described in the main text, helps to reduce uncertainty in model prediction. Also, we note that in the case of separate GPs for each coordinate, the correlation $\tilde{\rho}_{21}(s) = 0$ for any $s \in \mathcal{D}$, and the IUEA is proportional to the average product of pointwise standard deviations in the two coordinate directions.

In the extreme case where $\tilde{\sigma}_1^2(s) = \tilde{\sigma}_2^2(s) = \tilde{\rho}_{12}(s) = \tilde{\rho}_{21}(s)$, the ellipsoid degenerates and its volume is zero. In that case we obtain the usual notion of the width of a confidence interval.

I.4 GW

As a metric for registration, we use the Gromov-Wasserstein (GW) distance, which considers both overall uncertainty along with difficulty in alignment of two point sets (with multiplicity). While not directly suitable for comparing two curves, it is widely used for comparing “how close” two point clouds (as two degenerate distributions) are. Formally, the L_2 Gromov-Wasserstein distance (Solomon et al., 2021; Chowdhury and Mémoli, 2019) between two probability measures μ and ν defined on the same space M is defined as:

$$\text{GW}(\mu, \nu) := \inf_{\gamma \in \Gamma(\mu, \nu)} \int_{M \times M} \|x - y\|_2^2 d\gamma(x, y) = \inf_{\gamma \in \Gamma(\mu, \nu)} \mathbb{E}_\gamma \|X - Y\|_2^2, \quad (19)$$

where $\Gamma(\mu, \nu)$ denotes the collection of all measures on $M \times M$ with marginals μ and ν on the first and second component measures. When computing the GW distance between two finite, discrete datasets (as sampled from curves), $\mathbf{f}, \hat{\mathbf{f}}$, finite samples are treated as empirical measures consisting of one-point indicators.

We observe that this definition of GW shares similarities to IMSPE, but the distance is optimized over all possible bijective correspondences between point sets (rather than assuming a fixed correspondence). GW also shares similarities to ESD, but considers all possible bijections between point sets, as compared to ESD searching over all curve reparameterizations. We mainly use the GW metric for evaluating the registration quality in the main text. Computation of the GW metric is performed in Python using the `POT: Python Optimal Transport` module (Flamary et al., 2021), version 0.8.2.

J Practical Numerical Issues

J.1 Ordering and Labeling of Sample Points

We assume that the data comes in the form: $(y_{11}, y_{12}), (y_{21}, y_{22}), \dots, (y_{n1}, y_{n2})\}$. In this paper, we assume that these sample points are drawn from an underlying curve, and therefore, the stored $n \times 2$ array also conveys the order of observed points by the ordering of the n rows in this array. Since we are considering fitting closed curves, it is important that our proposed model is invariant to cyclic permutations (or re-labelings) of the ordering of these observed sample points (i.e., the ordering of the rows in the array), which shifts the point which is labeled the “starting point” (referred to as the seed in Supplementary Materials H).

This can be checked by fitting our GP model to cyclic permutations of observed sample points data, and checking that similar kernel hyperparameters and curve estimates are obtained. At the model level, this would suggest that the ordering we observe the sample points in does not affect the dependence characterized by the within-curve covariance kernel. Figure 19 shows bone fits using a multiple-output GP with the same set of $n = 15$ observed sample points, but designating a different starting point (in green). This means considering 15 cyclic permutations of the observed sample points. Note that the predicted mean and uncertainty ellipsoids are virtually identical, with any differences in evaluation metrics being due to the use of Algorithms 2 and 1 on the grid for which these predictions are evaluated. More crucially, the table at the bottom of the figure shows summaries of kernel hyperparameter estimate summaries under all cyclic permutations. All of the periodic

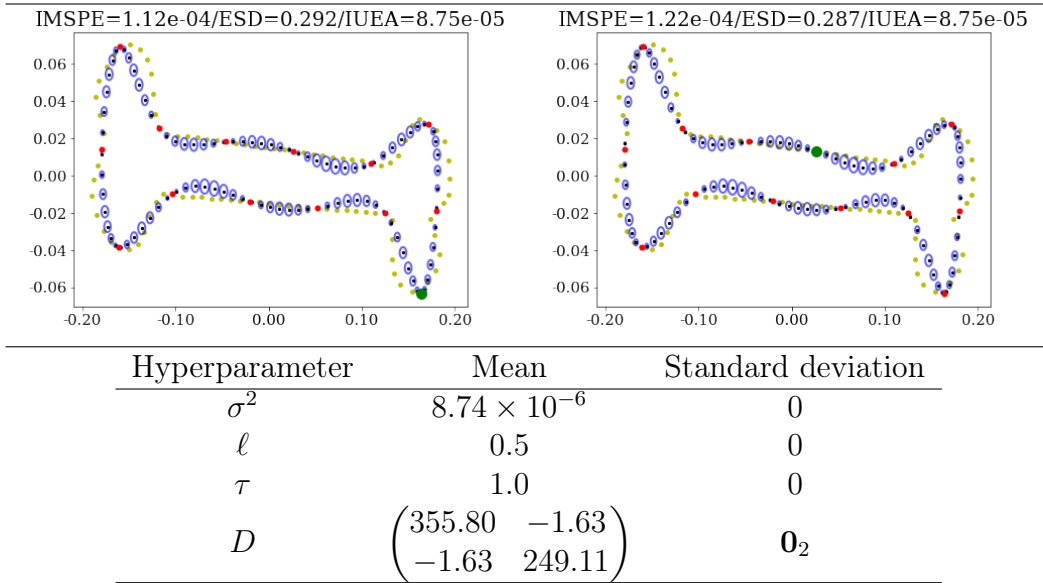


Figure 19: **GP model fits and hyperparameter estimates by starting point.** A bone curve from MPEG-7, modeled using a multiple-output GP with a periodic Matern 3/2 kernel. The top row shows fits for the same data, using two different starting points (in green); the bottom shows a table summarizing kernel hyperparameter estimates (variance σ^2 , length scale ℓ , period τ , between-coordinate coregionalization matrix D) when considering all 15 cyclic permutations of the starting point.

kernel hyperparameters, as well as the between-coordinate coregionalization matrix D , are estimated to be the same with no variance.

In addition, we also point out that when modeling multiple curves, the encoding method of each curve only affects estimates of kernel hyperparameters. For instance, labeling curves from two different groups as 1 and 2 or as 1 and 3 will lead to the same prediction mean obtained from fitting the GP model. This means that the curve label encoding does not affect the dependence characterized by the between-curve covariance kernel. By default, we use integer labeling (i.e., 0, 1, 2,...) for different outputs, to represent the coordinate function labels and/or sub-population labels. A detailed discussion of how categorical labeling can be modeled in GP regression is in Luo et al. (2022).

J.2 Numerical Issues in GP Regression

Numerical optimization for maximum likelihood estimation remains partially open at the time this paper is written (especially in high-dimensional domains), including interpolation error (Zaytsev et al., 2018) and simple parameter estimation (Basak et al., 2021).

As pointed out by Williams and Rasmussen (2006) (Section 5.4), when we fit a GP regression model by maximizing the joint likelihood, the multiple local maxima correspond to multiple hyperparameter estimates. Different hyperparameter estimates lead to different interpretations of the same data set. The specific case where the noise variance estimate is small compared to the magnitude of the mean (i.e., large signal-to-noise ratio) is known as kriging (Cressie, 2015). Kriging shows strong interpolation behavior in that the predictive mean curve from GP model fitting interpolates all data points. On the other hand, when

the noise variance is large compared to the magnitude of the mean (i.e., small signal-to-noise ratio), fits exhibit more smoothing behavior. We focus on the kriging aspect of GP regression within this manuscript, and point out that empirically, highly parameterized kernels (e.g., the separable kernel for multiple-output GPs as in Section 4) introduce more local maxima in the joint likelihood.

Gradient-based optimization methods, like L-BFGS-B, for maximizing joint likelihood generally involves specifying a step tolerance, since the GP likelihood can be numerically unstable under a multi-level periodic kernel. Periodicity introduces multiple local optima in the likelihood function, rendering the optimization problem difficult to solve. Even if the period is known, we recommend L-BFGS-B optimization using multiple initial points (also known as “restarts (of inner loop)” in the context of GP optimization). Although methods based on auto-differentiation (e.g., tensorflow with Adam) methods can provide more numerically stable results, it is more common to execute L-BFGS-B with multiple restart points.

Simulated annealing, as a global optimizer, seems to be more effective without the need for restarts. However, this approach can be computationally-intensive for GP fitting, especially when there are a quite a few kernel parameters to be estimated. However, we do note that simulated annealing is important for the landmark estimation task of Section 5.3, as the energy function being optimized often has multiple modes. As stated above, landmark estimation using standard gradient-based optimization approaches is not recommended due to its severe dependence on the initial point specified. The variational GP approach (with natural gradient) seems to work much less effectively compared to the aforementioned direct solvers based on L-BFGS-B and simulated annealing.

J.3 Restricted Kernel Hyperparameter Ranges

As mentioned above, the GP model typically requires some constraints to overcome numerical instabilities during optimization. If one specifies a periodic covariance kernel to fit a closed curve, a practical relationship which bounds the relationship between length scale and period hyperparameters is discussed in Section 3.2, based on the proof in Appendix D. By enforcing the kernel parameters to fall in this range and the noise variance to be small, we usually can obtain a reasonable minima which displays kriging behavior as discussed in Supplementary Materials J.2. For certain smooth kernels, such as the periodic radial basis function kernel, we have observed that it may be necessary to impose a constraint that the noise variance is small when fitting the model to obtain a kriging-type fit. Fixing this value to be within $(10^{-6}, 10^{-4})$ tends to resolve the issue in these cases when curves are adequately scaled.

If one does not use a periodic covariance kernel to fit a closed curve, we observe inconsistency especially when the arc-length passes the total curve length. Even if we want to consider parameters only within a period (arc-length parameter must be less than total curve length, which is unknown), further restrictions of kernel hyperparameters are likely necessary. The range to which hyperparameters are restricted will depend on the scale of the black-box function values. In practice, we assume that both the x and y coordinate function values fall in a finite range, say ± 10 after preprocessing. Accordingly, we restrict the Gaussian noise variance to $(10^{-6}, 10^{-4})$ to force the GP regression to interpolate.

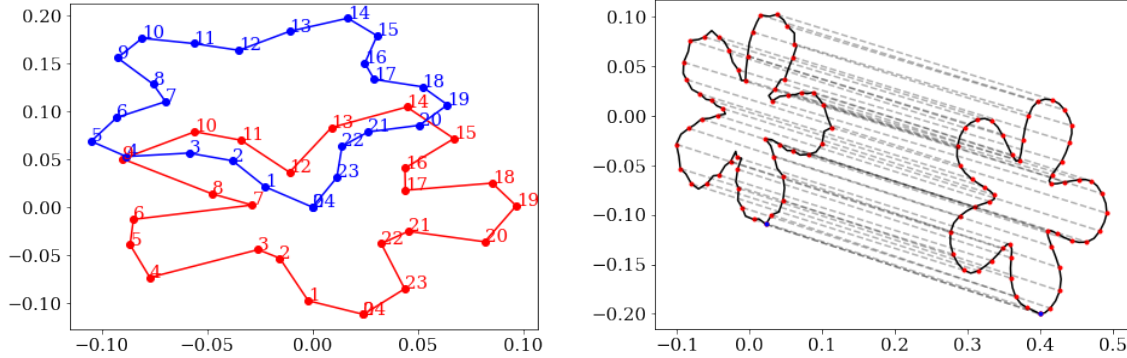


Figure 20: **Numerical issues with mapping between curve and SRVF in `fdasrsf` module.** (Left) Piecewise-linear curve (red) formed by 25 observed sample points (labeled by their respective ordering) drawn from a flower curve in MPEG-7, and resulting curve (blue) after transforming to its SRVF and then back to a curve. Points are annotated by index. (Right) Correspondence estimated by self-registration of flower curve observed at 101 sample points, perturbed by Gaussian noise, to itself.

J.4 Adding White Noise or Constant Kernels

In all examples throughout the paper, the full kernel used is typically the sum of a periodic covariance kernel with a white noise or constant kernel with very small lengthscale. This is equivalent to adding a diagonal perturbation matrix and helps to resolve numerical issues existing in the Cholesky factorization used for inversion of the covariance matrix. In general, adding a constant or white noise kernel with variance 10^{-3} is sufficient to avoid these issues. Based on experimentation in GP fitting for closed curves, we have found that adding the constant kernel typically resolves these issues more generally than the white noise kernel.

J.5 Mappings between Curve and SRVF

We have observed that mapping between curve and SRVF can result in some numerical errors which are exacerbated for curves which either have a relatively small number of observed sample points, or are observed with noise. In particular, the left panel shows a flower with 5 petals from the MPEG-7 dataset, with the red curve showing the original piecewise-linear curve formed by 25 observed points. Using version 2.2.9 of the `fdasrsf` module in Python for elastic shape analysis (Tucker, 2021), we simply apply the function which maps this curve to its SRVF, and then apply the function which maps this SRVF back to its curve representation. The resulting curve, shown in blue, has a drastically different shape than the original curve. In particular, it appears that this mapping tends to inaccurately reconstruct the points of high curvature between petals (e.g., points labeled 2 and 3), essentially smoothing out the resulting curve.

The right panel shows the correspondence induced by self-registration of the same flower with 5 petals, sampled at 101 points, and perturbed by Gaussian noise with standard deviation 0.008. By self-registration, we mean that we register this noisy curve to itself, with the goal of estimating a re-parameterization function that is the identity (up to small numerical differences) re-parameterization (i.e., a straight line with unit slope). While this

re-parameterization function estimated is indeed the identity, the mapping between SRVF and curve representation after this warping is applied has the effect of "smoothing out" the curve. These issues about the intrinsic weakness in the SRVF conversion should be taken into account when considering tasks involving elastic shape analysis using GP regression fits.